

**Inspection of copper canisters
for spent nuclear fuel by means
of ultrasound**

**Copper characterization,
FSW monitoring
with acoustic emission
and ultrasonic imaging**

Tadeusz Stepinski (editor),
Marcus Engholm, Tomas Olofsson
Uppsala University, Signals and Systems
Department of Technical Sciences, Sweden

August 2009

Svensk Kärnbränslehantering AB

Swedish Nuclear Fuel
and Waste Management Co

Box 250, SE-101 24 Stockholm
Phone +46 8 459 84 00



Inspection of copper canisters for spent nuclear fuel by means of ultrasound

Copper characterization, FSW monitoring with acoustic emission and ultrasonic imaging

Tadeusz Stepinski (editor),
Marcus Engholm, Tomas Olofsson
Uppsala University, Signals and Systems
Department of Technical Sciences, Sweden

August 2009

This report concerns a study which was conducted for SKB. The conclusions and viewpoints presented in the report are those of the authors and do not necessarily coincide with those of the client.

A pdf version of this document can be downloaded from www.skb.se.

Abstract

This report contains the research results concerning advanced ultrasound for the inspection of copper canisters for spent nuclear fuel obtained at Signals and Systems, Uppsala University in 2008. The first part of the report is concerned with aspects related to ultrasonic attenuation of copper material used for canisters. We present results of attenuation measurement performed for a number of samples taken from a real canister; two from the lid and four from different parts of canister wall. Ultrasonic attenuation of the material originating from canister lid is relatively low (less than 50 dB/m) and essentially frequency independent in the frequency range up to 5 MHz. However, for the material originating from the extruded canister part considerable variations of the attenuation are observed, which can reach even 200 dB/m at 3.5 MHz.

In the second part of the report we present further development of the concept of the friction stir welding process monitoring by means of multiple sensors formed into a uniform circular array (UCA). After a brief introduction into modeling Lamb waves and UCA we focus on array processing techniques that enable estimating direction of arrival of multimodal Lamb waves. We consider two new techniques, the Capon beamformer and the broadband multiple signal classification technique (MUSIC). We present simulation results illustrating their performance.

In the final part we present the phase shift migration algorithm for ultrasonic imaging of layered media using synthetic aperture concept. We start from explaining theory of the phase migration concept, which is followed by the results of experiments performed on copper blocks with drilled holes. We show that the proposed algorithm performs well for immersion inspection of metal objects and yields both improved spatial resolution and suppressed grain noise.

Contents

1	Introduction	1
2	Attenuation Estimation in the Extruded Canister Part	3
2.1	Introduction	4
2.2	Attenuation	4
2.2.1	Attenuation evaluation using buffer rod method	4
2.2.2	Diffraction correction	5
2.3	Samples and Measurement Setup	6
2.3.1	Measurement Setup	8
2.3.2	Results	9
2.3.3	Discussion	9
2.4	Resonant ultrasound spectroscopy	12
2.5	Conclusions	14
	Bibliography	14
2.A	Theory of the methods for attenuation evaluation	15
2.A.1	General consideration	15
2.A.2	Buffer rod method	16
2.A.3	Diffraction correction	17
3	Uniform Circular Arrays for Acoustic Emission	19
3.1	Introduction	20
3.2	Model	21
3.2.1	Uniform Circular Arrays	21
3.2.2	Signal model	22
3.2.3	Setup	23
3.3	Array processing of multimodal Lamb waves	23
3.3.1	Direction of Arrival Estimation	23
3.3.2	Beamformers	25
3.3.3	Broadband MUSIC	28
3.4	Simulation results	28
3.5	Discussion and conclusions	29

Bibliography	34
4 Efficient Algorithms for Synthetic Aperture Imaging	36
4.1 Introduction	37
4.2 Theory	38
4.2.1 Phase shift migration for the "exploding source" scenario	38
4.2.2 Adaptations to the case of pulse-echo measurements.	40
4.2.3 Summary of the algorithm	41
4.3 Experiments	42
4.3.1 Immersion test of copper block with side drilled holes and wire target . .	42
4.3.2 Immersion test of copper block with flat bottom holes	45
4.4 Conclusions and discussion	50
Bibliography	51
4.A Appendix	
Comments on the use of the discrete Fourier transform and aliasing	52

Chapter 1

Introduction

by Tadeusz Stepinski

In this report we are presenting our recent research results concerning ultrasonic inspection of copper canisters for spent nuclear fuel.

Our research activity in this project in 2008 was split into three separate tasks that are reported in the following chapters:

- Attenuation Estimation in the Extruded Canister Part,
- Uniform Circular Arrays for Acoustic Emission,
- Efficient Algorithms for Synthetic Aperture Imaging.

The first chapter deals with the investigation of variations of the ultrasonic attenuation in copper specimens originating from different canister parts. We present results of attenuation evaluation for copper samples taken from walls and lid of a real SKB canister. This is continuation of our previous work (TR-06-02) where the relationship between grain size and ultrasonic attenuation was examined experimentally on a set of copper blocks provided by the Corrosion and Metals Research Institute (KIMAB) where copper grains were artificially grown using thermal treatment.

A classical measurement setup with buffer rod operating in contact with the inspected material was applied for the attenuation measurements. Transducer diffraction effects were compensated to get absolute attenuation values. Considerable attenuation variations for the samples originating from different parts of canister wall were detected.

A simple resonant ultrasound spectroscopy test was also carried out to examine variation of the elastic properties of the investigated samples.

In the second chapter we present results of further investigation of uniform circular arrays (UCAs) sensing Lamb waves (LWs). We investigate three different array processing techniques for UCAs, two beamformers, and a high resolution technique capable of estimating direction of arrival (DOA). The first technique, proposed in our former report (TR-08-12), is a phase mode beamformer suitable for processing single-mode UCA signals. Two new techniques, the Capon beamformer and the broadband multiple signal classification technique (MUSIC), are proposed that belong to the class of high-resolution spectral estimation methods. Both techniques are capable of handling multi-mode signals and can be applied not only to UCA but to many other 2D array geometries. We compare performance of the investigated techniques using simulated multiple-mode signals.

In the final chapter we propose a phase shift migration algorithm for ultrasonic imaging of solids immersed in water. The proposed algorithm correctly treats ultrasonic waves propagating through layered media with different wave velocities and yields images with a high lateral resolution under such conditions.

Experiments were performed with copper blocks that showed that the lateral resolution in the reconstructed ultrasonic image is in principle independent of depth. It was also demonstrated that the proposed algorithm, along with the resolution improvement is capable of suppressing grain noise. The algorithm is implemented using fast Fourier transform (FFT) routines and our current implementation allows fast B-scans processing that takes shorter time than their acquisition.

Chapter 2

Attenuation Estimation in the Extruded Canister Part

by Tadeusz Stepinski

2.1 Introduction

The theoretical relationship between grain size and ultrasonic attenuation is well known and has been treated extensively in the literature. In our previous report [1] this relationship was examined experimentally on a set of copper blocks with artificially grown grains provided by the Corrosion and Metals Research Institute (KIMAB). Some discrepancies were observed concerning the attenuation as a function of grain size and some of the samples also proved to be anisotropic, which means that the material properties, such as wave velocity and attenuation, were dependent on the direction of propagation.

In this work a new set of samples originating from a real SKB canister was examined to investigate variations of the ultrasonic attenuation in copper specimens taken from different canister parts. A classical measurement setup with buffer rod operating in contact with the inspected material was applied for attenuation measurements.

Resonant ultrasound spectroscopy test was performed to examine variation of the elastic properties of the investigated samples.

In this report the theory of buffer rod method is shortly reviewed along with some practical issues concerning the use of this method. The attenuation of the inspected samples is presented in context of their metallographic structure.

2.2 Attenuation

It is well known that due to scattering of elastic waves ultrasonic attenuation is related to the grain size of a material. Roughly speaking, larger grains result in a higher attenuation of ultrasound. The relationship between attenuation α and grain size in the frequency range used for most ultrasonic inspections can be modeled by the following relation [2]:

$$\text{for } \lambda \gg 2\pi\bar{D}, \alpha \propto \bar{D}^3 f^4 \quad (2.1)$$

where \bar{D} is the average grain diameter, λ is the wavelength, and f is frequency.

The frequency region defined by Eq. 2.1 is referred to as *Rayleigh region*.

2.2.1 Attenuation evaluation using buffer rod method

The buffer rod method (BRM), proposed by E. P. Papadakis in 1968 [3, 4] was presented in detail in our previous report [1]. Here, we will include a short review needed for the presentation of recent results.

Ultrasonic attenuation in solids can be measured using the reflection and transmission effects of a plane wave (or a non-diffracted beam) at the planar interfaces including buffer/sample interface and specimen's back surface. However, since finite-sized aperture transducers are used in practical attenuation measurements the planar wave assumption does not hold. Consequently, the diffraction (beam spreading) effect has to be taken into account since it may cause considerable evaluation error, especially, when the BRM is used to evaluate attenuation in thick specimens using small aperture transducers. The beam spreading effect results in an apparent attenuation that is superimposed on the true material attenuation. Moreover, since the diffraction effects of a finite-sized transducer depend on wavelength, the error due to the apparent attenuation is also frequency dependent.

Thus, when absolute attenuation measurements are performed for thick specimens the diffraction correction has to be accounted for. The procedure of diffraction correction for attenuation

measurements using the BRM was first specified in 1973 by Papadakis [5].

The BRM method can be applied for both narrow-band and broad-band transducer excitations provided that the diffraction correction can be computed for the setup used in the measurement in the respective frequency band. The BRM method requires parallel front and back surfaces both for the buffer-rod and the specimen. Excessive roughness of the specimen's surfaces affects the measurements [6]. To facilitate understanding we present the BRM principle for a single frequency continuous wave excitation. However, in our experiments, the broad-band transducers were used and the processing was made in frequency domain for the Fourier transformed echoes.

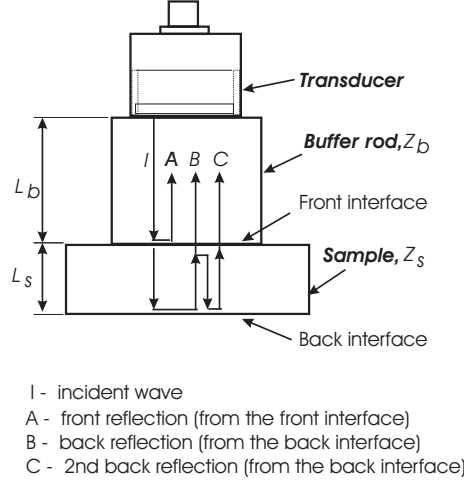


Figure 2.1: Setup used in buffer rod method. Back surface of the test specimen is in air.

Assume that a transducer sends a continuous ultrasonic wave with an amplitude of I and a frequency of f towards a specimen through an intermediate medium (buffer) in a setup shown in Fig. 2.1. If the specimen and buffer have different acoustic impedances the wave will be reflected at the front and back interfaces of the specimen. Assume that the amplitude of the echo from the front interface is $A = A(f)$, and the amplitudes of the first and second echoes from the back interface are $B = B(f)$ and $C = C(f)$, respectively (Fig. 2.1). The attenuation coefficient $\alpha = \alpha(f)$ of the sample with a length of L_s can be found from the measured amplitudes in the following manner (for details, see [5])

$$\alpha = \frac{1}{2L_s} 20 \log_{10} (R\tilde{B}) \quad [dB/m] \quad (2.2)$$

where the reflection coefficient R for the interface between buffer and sample is determined by $R = \sqrt{\frac{\tilde{A}/\tilde{B}}{\tilde{A}/\tilde{B}-1}}$; and $\tilde{A} = \frac{A}{B}$; $\tilde{B} = \frac{B}{C}$.

Eq. (2.2) is valid provided that bottom reflection of the ultrasound wave in the test sample is complete, which is quite accurately valid in air.

2.2.2 Diffraction correction

Diffraction correction is needed to compensate for beam spreading loss (diffraction loss). Generally, diffraction loss (DL) results in an estimation error, which depends on the sample thickness as well as on transducer size and frequency. As it was already mentioned, DL results in an "apparent attenuation" that adds to material attenuation. Therefore, DL leads to the overestimated values of attenuation.

Planar transducers and focused transducers of the same size have different beam patterns and the resulting diffraction correction for both types of transducers will be different. Calculating diffraction correction for a planar transducer is much easier than for the focused one. A universal DL curve, shown in Fig. 2.11 in Appendix, is plotted as a function of the normalized distance and, therefore, it can be applied to circular transducers with different radii and at different frequencies. In the present work the diffraction correction is performed for planar circular transducers used in our tests.

For broad-band excitation the diffraction correction has to be performed for each frequency in spectrums of the respective echoes, which means that the respective DL values need to be calculated first. Here, they were calculated in MATLAB based on the angular spectrum approach proposed in our previous works [7, 8]. The resulting curves corresponding to the echoes *A*, *B* and *C* in Fig. 2.1 are shown as a function of frequency in Fig. 2.2.

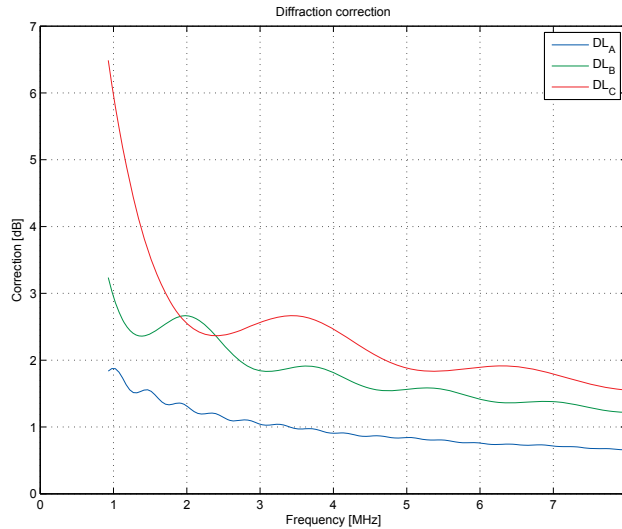


Figure 2.2: Diffraction loss corrections calculated for the echoes *A*, *B* and *C* in Fig. 2.1 as a function of frequency.

From Fig. 2.2 can be seen that the DL correction value increases with the distance from transducer and decreases with frequency. The calculated DL curves presented in Fig. 2.2 were introduced automatically into the attenuation evaluation (for details see Appendix 2.A).

2.3 Samples and Measurement Setup

Six copper blocks provided by the SKB's Canister Laboratory, specified in Table 2.1 were inspected. All blocks had the same dimensions 100x100x50 mm.

From Table 2.1 can be seen that the 2 blocks originated from canister lid while the remaining ones were from the canister extruded part. Preliminary ultrasonic inspection showed that ultrasonic attenuation of the blocks varied considerably.

Small samples were cut out from the 3 blocks as indicated in Table 2.1 for metallographic examination of their structure and resonance spectroscopy test. The small samples were polished and their microstructure in the plane normal to ultrasonic wave propagation was investigated using optical microscope; selected micrographs are presented in Fig. 2.3. Rough estimation of grain size resulting from that examination is listed in Table 2.1.

SKB Cu block	Attenuation	Sample	Material	Approx grain size in μm
<i>Tx184 2C-R100</i>	low	1	lid	50-100
<i>Tx184 2C-R300</i>	low	-	lid	
<i>T53-2 1050-88A</i>	low	-	lid	
<i>T53-2 1050-88B</i>	low	2	lid	100-200
<i>T53-2 920-238A</i>	high	-	extruded	
<i>T53-2 920-238B</i>	high	3	extruded	200-400

Table 2.1: Features of the inspected copper cubes.

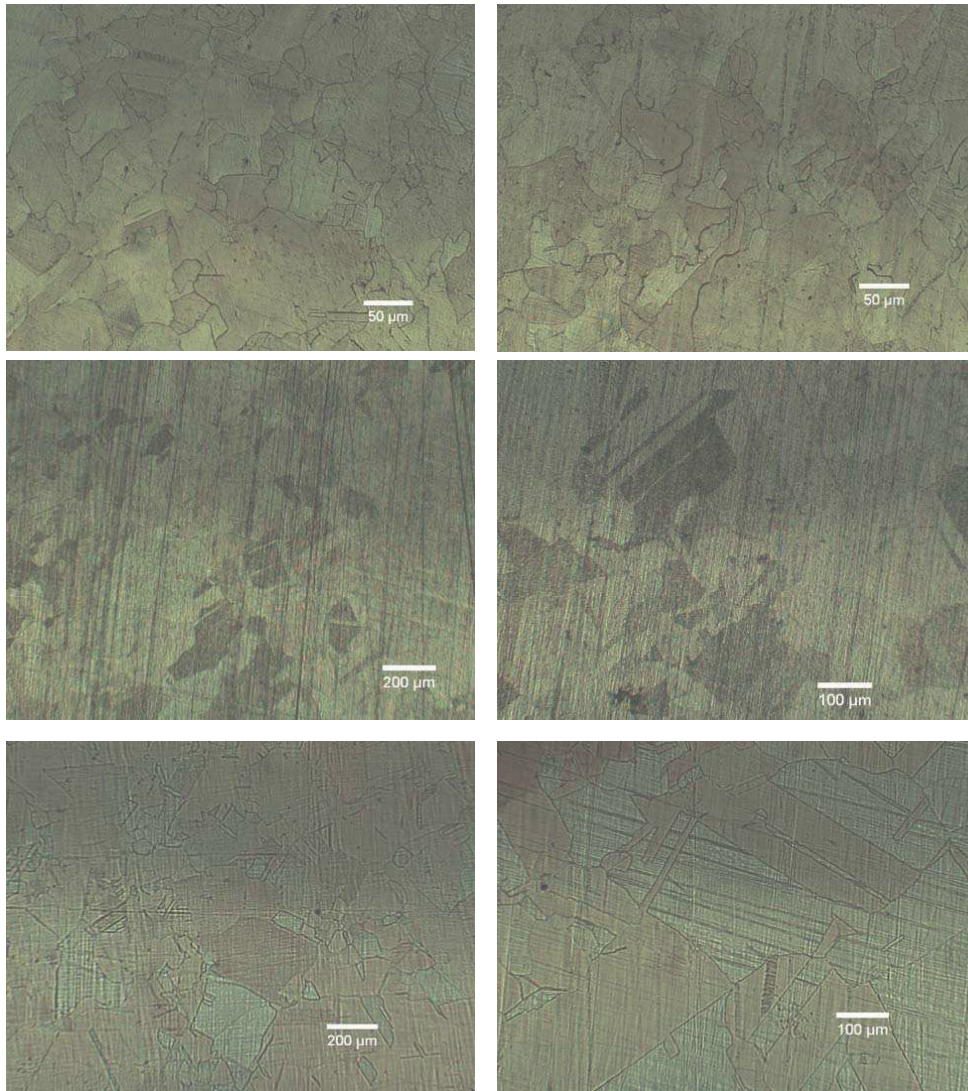


Figure 2.3: Micrograph of the samples, from above, sample 1, 2 and 3, respectively.

From Fig. 2.3 can be seen that the samples have not only different grain size but also various structures, the structure of samples 1 and 2, originating from a forged canister lid, is different from that of sample 3, which was cut out from an extruded tube.

2.3.1 Measurement Setup

Buffer rod setup for the attenuation measurement in air, shown in Fig. 2.4 was designed for our experiments. The setup consists of a specially designed transducer which can be permanently assembled with a buffer rod made of Rexolite, which is a polystyrene plastic. The Rexolite buffer has a threaded washer on its top, matched to the transducers thread. The acoustic contact between the transducer and the buffer is provided by a standard ultrasonic gel. The other buffer end is placed in contact with an inspected sample. To minimize the diffraction effects a relatively large transducers (1" aperture) were used. Two specially designed transducers with different center frequencies (3 MHz and 5MHz) from ValpeyFisher, USA, were used in our experiments. The transducers' frequency responses (Fourier transform of the buffer rod bottom echo in the air) are shown in Fig. 2.5. Details concerning the buffer rod setup are listed in Table 2.2.

	Diameter [mm]	Hight [mm]
Buffer rod	60	35
Transducer 3 MHz	25,4	25
Transducer 5 MHz	25,4	25

Table 2.2: Dimensions of the test setup



Figure 2.4: Buffer rod setup used for the attenuation evaluation.

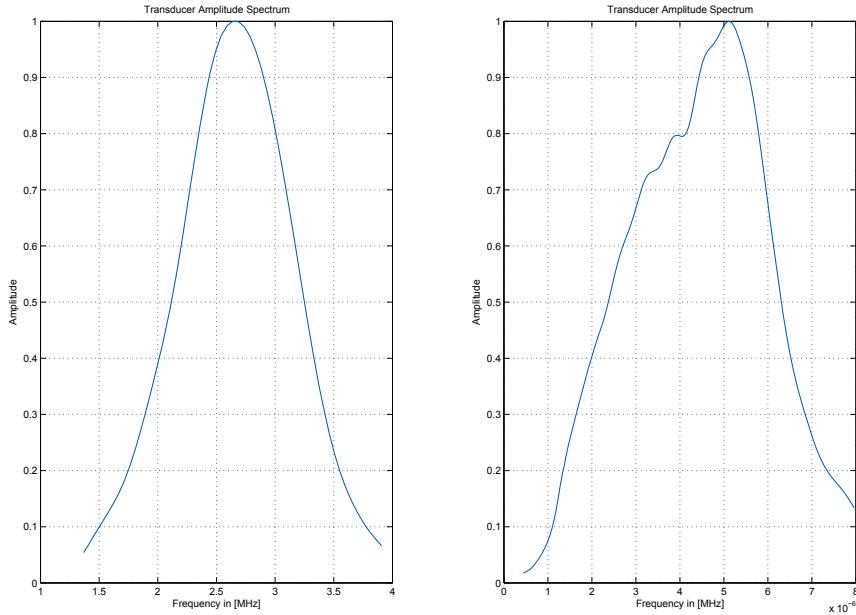


Figure 2.5: Frequency responses of the two transducers used in the attenuation measurements. 3MHz transducer (left) and 5MHz transducer (right).

2.3.2 Results

Attenuation evaluation was performed for all 6 blocks using the buffer rod setup shown in Fig. 2.4. The Buffer rod was placed on the top of each sample and the acoustic contact was provided using a standard ultrasonic gel. All three echoes (*A*, *B* and *C* shown in Fig. 2.1) were acquired without moving the transducer using the digital ultrasonic plug-in board *USPC3100LA* from Socomate International, France. Gain settings were adjusted to utilize the full dynamic range of the AD converter at the USPC board. The echoes, sampled with frequency 100 MHz were stored in a PC. Later those echoes were transferred to MATLAB for processing in frequency domain. The diffraction correcting curves shown in Fig. 2.2 were introduced in the calculations. The measurement procedures were performed for two frequency bands:

- Lower frequency band using the 3MHz transducer, and
- Higher frequency band using the 5MHz transducer.

Results are presented in two different forms as a function of frequency, the attenuation coefficient α in dB/m in Fig. 2.6, and the ratio of the amplitude spectra of two successive bottom echoes in Fig. 2.7. Amplitude ratios of the same echoes estimated using both transducers in time domain are listed in Table 2.3.

2.3.3 Discussion

From Figs. 2.6 and 2.7 can be seen that the samples originating from the extruded canister part (*1050-88* and *920-238*) have generally higher attenuation than those from the canister lid (*R-100* and *R-300*). Attenuation of the low attenuating samples, i.e., *1050-88*, *R-100* and *R-300*,

is more or less constant in the whole frequency band (from 1.8 to 4 MHz) and does not exceed 100 dB/m or 3 dB in the echo amplitude ratio for 50 mm.

The lid samples are the least attenuating of all the investigated samples with an average attenuation less than 50 dB/m. Their attenuation seems to decrease with frequency in the frequency band 1.8 to 3.5 MHz, which is probably due to the overestimation of diffraction effects. Note, that the corresponding change of amplitude ratio in that band in Fig. 2.7 is less than 1 dB.

The samples from the extruded part have generally higher (1050-88) or even much higher attenuation (920-238) than those from the lid. Attenuation of the samples 1050-88 is more or less constant and equal approx. 70-80 dB/m (or 2.1-2.5 dB in the echo amplitude ratio for 50 mm) in the whole investigated frequency range. Attenuation of the samples 920-238 is very high and its frequency dependence is well pronounced, it starts with 100 dB/m at 1.8 MHz and approaches 250-350 dB/m at 4 MHz. The corresponding echo drop in time domain is in the range of 12 dB for the 3 MHz transducer and 17 dB for the 5 MHz transducer (see Table 2.3). The attenuation coefficients measured for both 920-238 samples show substantial differences in the higher frequency band. (Note, however, that the second bottom echoes (C-echoes) measured for the 920-238 with the 5MHz transducer were quite weak and noisy.)

Summarizing, we can say that a substantial attenuation difference has been observed between the canister samples originating from the canister extruded part; both values of the attenuation coefficient α and its frequency dependence are quite different for the samples 1050-88 and 920-238 despite apparently small difference in grain size (Table 2.1).

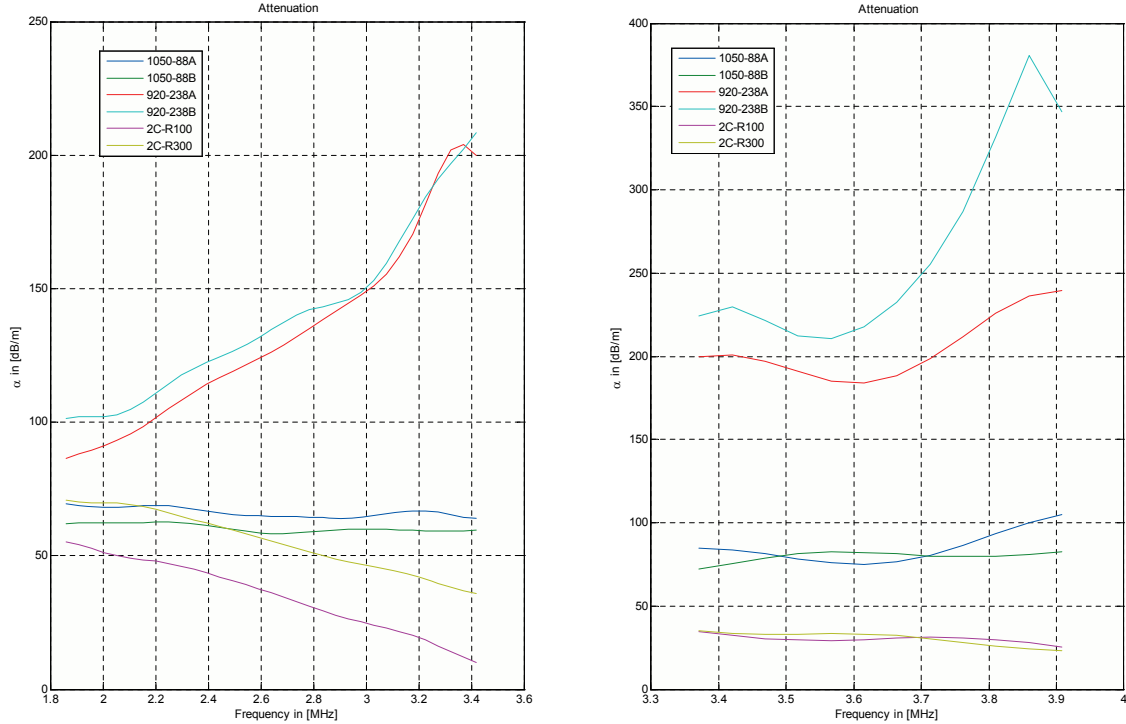


Figure 2.6: Estimated attenuation coefficients α in dB/m. Obtained using the 3MHz transducer (left) and 5MHz transducer (right). Note different scales at both plots.

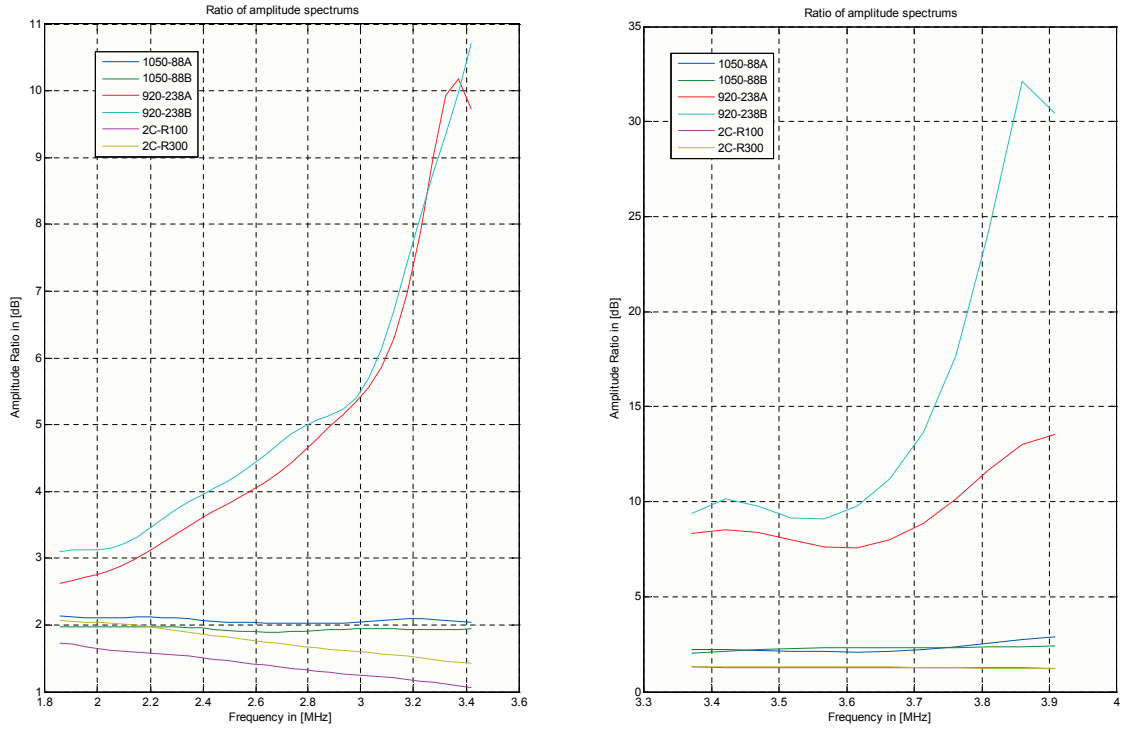


Figure 2.7: Amplitude ratios between the two successive sample bottom echoes in dB as a function of frequency. Obtained using the 3MHz transducer (left) and 5MHz transducer (right). Note different scales at both plots.

Block	Transducer 3 MHz	Transducer 5 MHz
1050-88A	6.24 dB	8.43 dB
1050-88B	5.75 dB	6.87 dB
920-238A	11.34 dB	17.31 dB
920-238B	12.29 dB	16.36 dB
2C-R100	2.54 dB	3.71 dB
2C-R300	4.57 dB	4.39 dB

Table 2.3: Amplitude ratios between the two successive bottom echoes of the inspected samples.

2.4 Resonant ultrasound spectroscopy

In a resonant ultrasound spectroscopy (RUS) test, mechanical resonance frequencies of an object in the ultrasound frequency range are measured. Resonance frequencies corresponding to various vibration modes are related to the material properties of an object, such as geometric and elastic properties. Resonance frequencies of an object with arbitrary geometry and given elastic properties can be relatively easily calculated using numerical methods. Elastic constants of the inspected material can be found numerically from the measured RUS spectrum by solving so called inverse problem.

In our former report [9] we presented theory behind RUS as well as our results obtained for the copper samples with artificially grown grains. We found that the correlation between the elastic constants estimated in the RUS experiment and the grain size was weak.

Here, we perform only a simple RUS test to check whether the features of the presently investigated samples affect one of the main resonances.

The setup used in the test, shown in Fig. 2.8, consisted of a pair of specially designed piezoelectric transducers (transmitter and receiver) and a network analyzer (Agilent 4395A). An amplifier was also used to amplify weak signals from the receiver. Three copper specimens taken from the same blocks as those used for the metallographic inspection were used in the test (see Table 2.1). The specimens had identical dimensions 30x28x25 mm.

Resonance frequencies of the specimens were calculated using typical copper elastic constants. A vibration mode suitable for the RUS test was chosen from the list of resonance frequencies. This mode, which is illustrated in Fig. 2.9, is characterized by a relatively high particle displacement at the specimen corners. Such mode should be easily detected in the setup shown in Fig. 2.8. Additionally, since this mode, located theoretically at approx. 88 kHz, was quite isolated it could not be easily mixed up with neighbor resonances. The corresponding, strongly pronounced resonance mode was found experimentally at approx. 86 kHz, see Fig. 2.10. From Fig. 2.10 can be seen that the frequencies of that mode measured for all 3 specimens are almost identical, the maximum difference that appears between the specimen 1050-88 (the highest) and 920-238 (the lowest) is only approx. 70 Hz.

An obvious conclusion can be drawn that the elastic constants of all specimens are very similar.

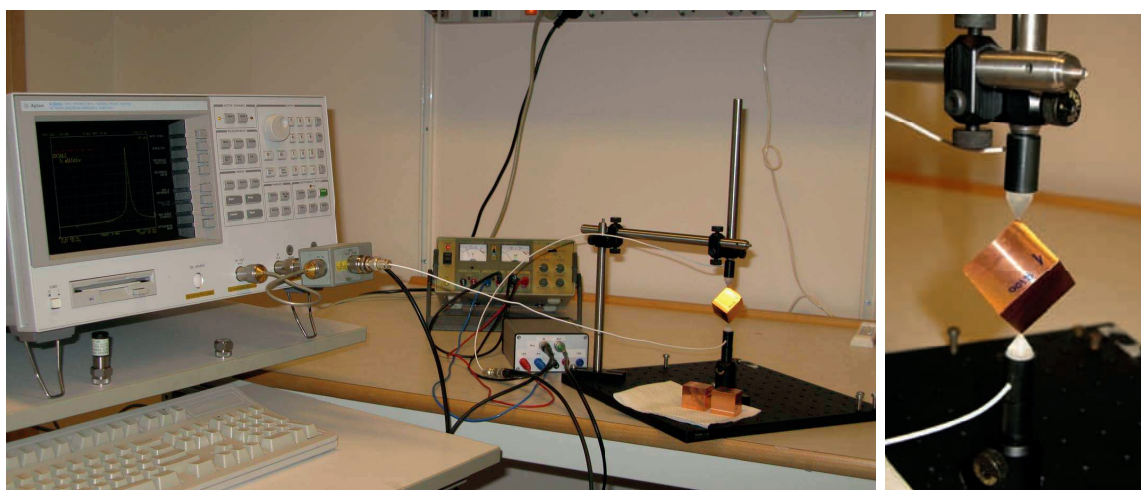


Figure 2.8: RUS test setup used in the experiment.

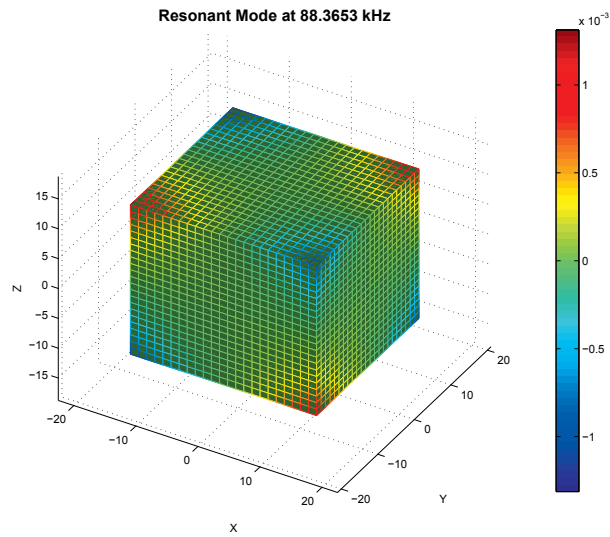


Figure 2.9: Vibration mode investigated in the RUS experiment.

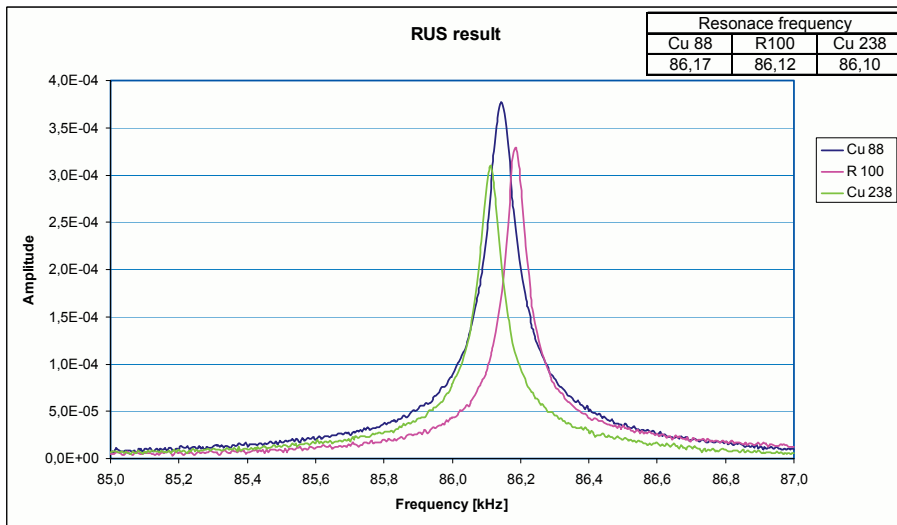


Figure 2.10: Result of the RUS experiment. Upper-right corner: resonance frequencies measured for the samples in kHz.

2.5 Conclusions

Ultrasonic attenuation was evaluated for 6 copper blocks originating from a real SKB's canister. Buffer rod method with diffraction loss compensation was used to obtain absolute values of the attenuation in function of frequency. The method yielded consistent results in two frequency bands for similar copper material.

It was found that the material originating from canister lid is characterized by a relatively low attenuation (less than 50 dB/m) that is essentially frequency independent in the frequency range from 1 to 5 MHz.

However, the material originating from the extruded canister part displays considerable variations of the attenuation, which varies from approx. 70 dB/m to approx 200 dB/m at 3.5 MHz. Those attenuation variations may result in the variations in the bottom echo amplitudes at 50 mm as high as 6 dB for a 3 MHz transducer and 8 dB for a 5 MHz transducer. This means that the amplitude based defect sizing based on a constant amplitude threshold would be completely unreliable in such material.

A simple RUS test performed for three different copper specimens did not show any essential difference in the elastic constants.

Bibliography

- [1] T. Stepinski (editor), F. Lingvall, and E. Wennerström. Inspection of copper canisters for spent nuclear fuel by means of ultrasound - synthetic aperture imaging, evaluation of ultrasonic attenuation in copper. Technical Report TR-06-02, SKB, 2006.
- [2] E.P. Papadakis. Ultrasonic attenuation caused by scattering in polycrystalline metals. *Journal of the Acoustical Society of America*, 37(4):711 – 717, 1965.
- [3] E. P. Papadakis. Ultrasonic attenuation in thin specimens driven through buffer rods. *J. Acoust. Soc. Am.*, 44(3):724–734, 1968.
- [4] E. P. Papadakis. Buffer-rod system for ultrasonic attenuation measurements. *J. Acoust. Soc. Am.*, 44(5):1437–1441, 1968.
- [5] E. P. Papadakis, K. A. Fowler, and L. C. Lynnworth. Ultrasonic attenuation by spectrum analysis of pulses in buffer rods: Method and diffraction corrections. *J. Acoust. Soc. Am.*, 53:1336–1343, 1973.
- [6] P.B. Nagy and L. Adler. Scattering induced attenuation of ultrasonic backscattering. *Rev. of Progr. in Quantitative NDE.*, 7:1263–1271, 1988.
- [7] P. Wu, F. Lingvall, and T. Stepinski. Inspection of copper canisters for spent nuclear fuel by means of ultrasonic array system - electron beam evaluation, modelling, and materials characterization. Technical Report TR-99-43, SKB, 1999.
- [8] P. Wu, F. Lingvall, and T. Stepinski. Inspection of copper canisters for spent nuclear fuel by means of ultrasound - electron beam evaluation, harmonic imaging, materials characterization and ultrasonic modelling. Technical Report TR-00-23, SKB, 2000.
- [9] T. Stepinski (editor), M. Engholm, and T. Olofsson. Inspection of copper canisters for spent nuclear fuel by means of ultrasound - FSW monitoring with acoustic emission, copper characterization and ultrasonic imaging. Technical Report TR-08-12, SKB, 2008.

2.A Theory of the methods for attenuation evaluation

2.A.1 General consideration

The buffer rod method (BRM) and the immersion method (IM) used for attenuation estimation apply the same theory. In both methods an intermediate medium between the transducer and the inspected sample is placed, the reflections (echoes) from the sample's front and back surfaces are used for the evaluation of attenuation. In attenuation evaluation, the reflection and transmission coefficients for plane waves are used which may lead to some error. Both methods require parallel surfaces in the buffer as well as in the sample. The difference of the two methods lies in that the BRM has the back surface in air whereas the IM has the back surface in the immersing fluid so that the reflection from the back surface in the IM is not assumed to be ideal (meaning total reflection) as in the BRM.

Here, we present a general theory which applies for any case when the sample's back surface may have contact with any material, such as, air, water, or any other fluid or solid.

Referring to Fig. 2.1, we assume that the acoustic impedances of the buffer rod and the sample are Z_b and Z_s , respectively. Then, the reflection coefficients at the buffer/sample interface and the sample/buffer interface, $R_{bs} \equiv R$ and R_{sb} , can be written, respectively, as

$$R = R_{bs} = \frac{Z_s - Z_b}{Z_s + Z_b} \quad (2.3)$$

$$R_{sb} = \frac{Z_b - Z_s}{Z_b + Z_s} = -R \quad (2.4)$$

and the transmission coefficients at the buffer/sample and the sample/butter interfaces, T_{bs} and T_{sb} , can be expressed, respectively, as

$$T_{bs} = \frac{2Z_s}{Z_b + Z_s} \quad (2.5)$$

$$T_{sb} = \frac{2Z_b}{Z_s + Z_b} \quad (2.6)$$

From Eqs. (2.3) to (2.6) it is easy to find that

$$T_{bs}T_{sb} = 1 - R^2 \quad (2.7)$$

Furthermore, letting R_{back} be the reflection coefficient at the sample's back interface, and assuming that the incident wave has an amplitude of $I = I(f)$ at frequency f and the sample has an attenuation α in Nepers/m, we may find the front reflection from the sample's front surface, $A = A(f)$,

$$A = IR \quad (2.8)$$

the back reflection from the sample's back surface, $B = B(f)$,

$$\begin{aligned} B &= IT_{bs}R_{back}T_{sb}e^{-2\alpha L_s} \\ &= I(1 - R^2)R_{back}e^{-2\alpha L_s} \end{aligned} \quad (2.9)$$

and the 2nd back reflection from the back surface (noting the relation $R_{sb} = -R$ in Eq. (2.4)), $C = C(f)$,

$$\begin{aligned} C &= IT_{bs}R_{back}R_{sb}R_{back}T_{sb}e^{-4\alpha L_s} \\ &= -IR(1 - R^2)R_{back}^2e^{-4\alpha L_s} \end{aligned} \quad (2.10)$$

The ratio of the front echo and the back echo follows from Eqs. (2.8) and (2.9)

$$\tilde{A} = \frac{A}{B} = \frac{R}{(1 - R^2)R_{back}e^{-2\alpha L_s}} \quad (2.11)$$

The ratio of the first back echo and the second back echo can be written, from Eqs. (2.9) and (2.10), as

$$\tilde{B} = \frac{B}{C} = \frac{1}{-RR_{back}e^{-2\alpha L_s}} \quad (2.12)$$

From $\tilde{A}/\tilde{B} = -R^2/(1 - R^2)$, we can find the reflection coefficient from A and B (that are available from measurements), as follows

$$R = \sqrt{\frac{\tilde{A}/\tilde{B}}{\tilde{A}/\tilde{B} - 1}} \quad (2.13)$$

When R is determined, the corrected attenuation coefficient can be found from Eq. (2.12) as follows

$$\alpha = \frac{1}{2L_s} 20 \log_{10} \left[-RR_{back}\tilde{B} \right] \quad (2.14)$$

where α is in dB/m. An alternative form to find the attenuation coefficient α can be obtained from Eq. (2.11),

$$\alpha = \frac{1}{2L_s} 20 \log_{10} \left[\frac{(1 - R^2)R_{back}}{R} \tilde{A} \right] \quad (2.15)$$

Re-writing Eqs. (2.14) and (2.15) in the following manner,

$$\alpha = \frac{1}{2L_s} 20 \log_{10} [-RR_{back}] + \frac{1}{2L_s} [20 \log_{10}(B) - 20 \log_{10}(C)] \quad (2.16)$$

$$\alpha = \frac{1}{2L_s} 20 \log_{10} \left[\frac{(1 - R^2)R_{back}}{R} \right] + \frac{1}{2L_s} [20 \log_{10}(A) - 20 \log_{10}(B)] \quad (2.17)$$

we can easily find that the buffer rod method is essentially the logarithmic spectral difference method that takes into account the reflection from the front and back interfaces. Eq. (2.16) is the logarithmic spectral difference method based on the spectra of the 1st back and 2nd back echoes for broad band measurement. Eq. (2.17) is the logarithmic spectral difference method based on the spectra of the front and 1st back echoes.

2.A.2 Buffer rod method

If the back surface is in air, then it is reasonable to assume $R_{back} \approx -1$, which means a total reflection from the back surface. In this case, Eq. (2.14) becomes

$$\alpha = \frac{1}{2L_s} 20 \log_{10} \left[R\tilde{B} \right] \quad (2.18)$$

which is the existing buffer rod method. Eq. (2.15) becomes

$$\alpha = \frac{1}{2L_s} 20 \log_{10} \left[\frac{-(1 - R^2)}{R} \tilde{A} \right] \quad (2.19)$$

2.A.3 Diffraction correction

The diffraction of a transducer will be one of the main sources causing error in attenuation estimation, especially when the BRM and IM are used to evaluate attenuation for thick materials. The loss due to diffraction (or beam spreading) will result in apparent "attenuation". The correction of this error, known as diffraction correction, was made presently only for planar transducers. To realize the diffraction correction, one needs to calculate diffraction loss (DL). For planar circular transducer, one normalized DL curve like in Fig. 2.11 is sufficient for correcting diffraction error for transducers with different radii at different frequencies. When the DL curve is available, the diffraction correction can be made using the following procedure.

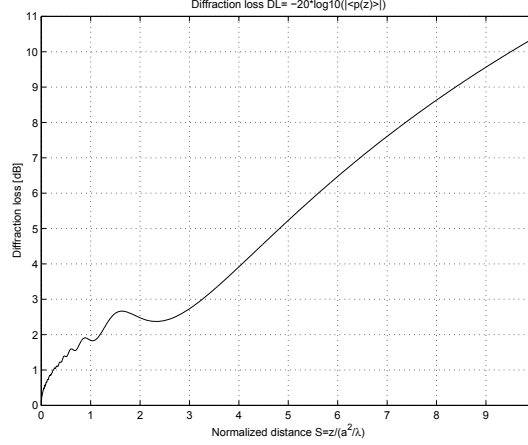


Figure 2.11: Diffraction loss in dB as a function of normalized distance $S = z/(a^2/\lambda)$. Note that the normalized distance S is frequency dependent.

First, determine the distances of the front interface echo, the 1st and the 2nd back interface echoes, which are normalized by $z_b = a^2/\lambda_b$ in the buffer and $z_s = a^2/\lambda_s$ in the sample,

$$S_A = \frac{2L_b}{z_b} = \frac{2L_b}{(a^2/\lambda_b)} = \frac{2L_b c_b}{a^2 f} \quad (2.20)$$

$$S_B = \frac{2L_b}{z_b} + \frac{2L_s}{z_c} = \frac{2L_b}{(a^2/\lambda_b)} + \frac{2L_s}{(a^2/\lambda_s)} = \frac{2L_b c_b}{a^2 f} + \frac{2L_s c_s}{a^2 f} \quad (2.21)$$

$$S_C = \frac{2L_b}{z_b} + \frac{4L_s}{z_c} = \frac{2L_b}{(a^2/\lambda_b)} + \frac{4L_s}{(a^2/\lambda_s)} = \frac{2L_b c_b}{a^2 f} + \frac{4L_s c_s}{a^2 f} \quad (2.22)$$

where $\lambda_b = c_b/f$ and $\lambda_s = c_s/f$ are the wave lengths, and c_b and c_s are the sound speeds in the buffer and the sample, respectively.

Secondly, get the DL values in the DL curve in Fig. 2.11 at the above three distances S_A , S_B and S_C , and then use the following relations to compensate for diffraction loss for all the echoes' amplitudes, A , B and C ,

$$A_c = A \cdot 10^{DL_A/20} \quad (2.23)$$

$$B_c = B \cdot 10^{DL_B/20} \quad (2.24)$$

$$C_c = C \cdot 10^{DL_C/20} \quad (2.25)$$

Finally, for BRM, substitute DL_A , DL_B and DL_C for A , B , C in Eqs. (2.13), (2.18) and (2.19),

and get the corrected attenuation coefficient

$$\tilde{\alpha} = \frac{1}{2L_s} 20 \log_{10} \left(R_c \tilde{B}_c \right) \quad (2.26)$$

and the alternative form

$$\tilde{\alpha} = \frac{1}{2L_s} 20 \log_{10} \left[\frac{-(1 - R_c^2) \tilde{A}_c}{R_c} \right] \quad (2.27)$$

and for IM, substitute DL_A , DL_B and DL_C for A , B , C in Eqs. (2.13), (2.16) and (2.17), and get the corrected attenuation coefficient

$$\tilde{\alpha} = \frac{1}{2L_s} 20 \log_{10} \left(R_c^2 \tilde{B}_c \right) \quad (2.28)$$

and the alternative form

$$\tilde{\alpha} = \frac{1}{2L_s} 20 \log_{10} \left[-(1 - R_c^2) \tilde{A}_c \right] \quad (2.29)$$

where

$$R_c = \sqrt{\frac{\tilde{A}_c / \tilde{B}_c}{\tilde{A}_c / \tilde{B}_c - 1}} \quad (2.30)$$

$$\tilde{A}_c = \frac{A_c}{B_c} \quad (2.31)$$

$$\tilde{B}_c = \frac{B_c}{C_c} \quad (2.32)$$

Chapter 3

Uniform Circular Arrays for Acoustic Emission

by Marcus Engholm

3.1 Introduction

Lamb waves (LW) offer a number of advantages in structural health monitoring (SHM) applications, especially in those situations where large areas of thin-walled structures are to be monitored. LWs can be used as an active testing method capable of detecting and locating damage as well as, in some cases, estimating its severity. Inspection using LWs is also a well-established industrial test method used in nondestructive evaluation (NDE). In NDE LWs are commonly excited and received using a pair of handheld transducers that are scanned over an inspected structure. In SHM a sensor and actuator network is integrated with the monitored structure to assess the state of the structure during operation. Information about damage can be obtained from various characteristics of the received signals, such as, propagation time, amplitude or frequency content. However, in LW applications where large areas are to be assessed, accurate detection and localization of the damage generally requires a large and dense network of actuator-sensor pairs.

One way of reducing the number of LW sensors in a SHM network is using more sophisticated sensors capable of "directional sweeping" larger areas without moving the transducers. The "sweeping" can be performed using techniques that have been developed for phased arrays (PA). Phased array instruments, that are well-established in NDE, enable rapid scanning of large inspected volumes using multiple transducer arrays steered by specialized electronics both in transmission and reception. The most common are linear phased arrays that consist of a number of active transducers arranged in a line. The use of such arrays for SHM was proposed by Giurgiutiu & Bao [1] who coined the name *embedded-ultrasonic structural radar* (EUSR). In the EUSR concept the LWs are generated over a long range using a number of piezoelectric wafers arranged into a uniform line array and integrated with the inspected plate-structure. The array is used both for transmission and reception of LWs in a pulse-echo mode, using electronics operating in a delay-and-sum (DAS) scheme in time-domain. As a result a relatively narrow beam pattern can be generated and used for angle-scanning a large surface. Damages detected in the structure can be localized based on the beam's azimuth and time of arrival of the received echoes. A large number of LW transducers in a dense sensor network would preferably be replaced by a few but more complex and sophisticated EUSRs.

A detailed investigation of linear phased array beamforming concepts in application to SHM can be found in [2] where a study of spatial characteristics of linear arrays is presented. Also Giurgiutiu in his most recent book [3] presents both simulated and experimental results concerning sensitivity of the EUSR used for detecting cracks in plates. It appears, not entirely unexpected, that the linear array based EUSR has certain essential disadvantages: firstly, it does not cover the whole azimuth range (0° to 360°) since its angular resolution depends on the steering angle, it is best in the direction normal to the array and it is very poor at the angles close to 0° and 180° (endfire). Secondly, linear arrays are suffering from the front-back ambiguity (mirror effect), which makes it impossible to discriminate targets located in front of the array and behind it.

To overcome the above mentioned disadvantages inherent to the 1-D linear arrays Giurgiutiu considers rectangular and circular 2-D array configurations [3]. The use of 2-D circular arrays for LW SHM was proposed already in 1998 by Wilcox [4] who presented the idea of a circular array composed of six PVDF¹ interdigital transducers with curved fingers, each of them generating a divergent beam enabling inspection of a pie-slice shaped area of the plate. Wilcox et al. [5] investigated circular arrays with ceramic-disc actuators for long range LW SHM in isotropic plate structures and they found that the area of the inspected plate to the area of the circular array was as large as 3000 : 1. Wilcox further developed those ideas and proposed a general approach

¹PVDF is an abbreviation for Polyvinylidene Fluoride which is a piezoelectric polymer.

for processing data from a LW transducer array for omnidirectional guided wave arrays, refined for a class of circular arrays [6, 7]. Following this line, Fromme et al. [8] presented experimental results obtained using a compact, low power array employing piezoelectric transducer elements acting as point sources and receivers.

We previously proposed the concept of phase mode beamformers for uniform circular arrays (UCAs) consisting of a number of LW transducers evenly distributed on a circle [9, 10]. A UCA is not only omnidirectional but its beampattern in the azimuth plane is essentially independent of the steering angle. The desired beam shape can be achieved if the outputs of all array elements are fed to a structure, referred to as beamformer. A phase mode excitation beamformer, based on Fourier analysis of the array excitation function enables pattern synthesis for UCAs using methods normally associated with linear phased arrays.

Authors of the above-cited works avoided addressing a very difficult issue related to the multimodal nature of LWs by assuming single mode LWs with a priori known characteristics. However, depending on the frequency of the signal and the thickness of the plate, two or more LW modes can be excited. Both the dispersive properties of LWs as well as the existence of multiple propagation modes create difficulties during processing the received data. Many researchers have designed their measurement setups to reduce the interference of unwanted modes.

In this report, three techniques for array processing of LWs using UCAs are presented, two beamformers, and a high resolution technique aimed for direction of arrival (DOA) estimation. The first technique, previously proposed by us, is a phase mode beamformer suitable for processing single-mode UCA signals. Beampattern design using a beamspace representation of the array manifold vector is explained. The two remaining techniques, the Capon beamformer and the broadband multiple signal classification technique (MUSIC), belong to the class of high-resolution spectral estimation techniques. They are capable of handling multi-mode signals and can be applied to arbitrary array geometries. Moreover, they require no prior information about the characteristics of the material. Performance of all considered here techniques is compared using simulated multiple-mode signals.

3.2 Model

3.2.1 Uniform Circular Arrays

A UCA, as shown in Figure 3.1, consists of M equally spaced array elements located on a circle. One of the greatest advantages with UCAs are their 360° azimuth coverage with an essentially unchanged beam pattern in all directions. Although not of concern in this work, UCAs are also capable of elevation directivity.

The array manifold vector of a M -element uniform circular array with radius R for an incoming plane wave with wavenumber k and incident angle θ is defined as [11]

$$\mathbf{a}(\theta, k) = \begin{bmatrix} e^{-jkR \cos(\theta)} \\ e^{-jkR \cos(\theta - \gamma_c)} \\ \vdots \\ e^{-jkR \cos(\theta - (M-1)\gamma_c)} \end{bmatrix}, \quad (3.1)$$

where $\gamma_c = 2\pi/M$.

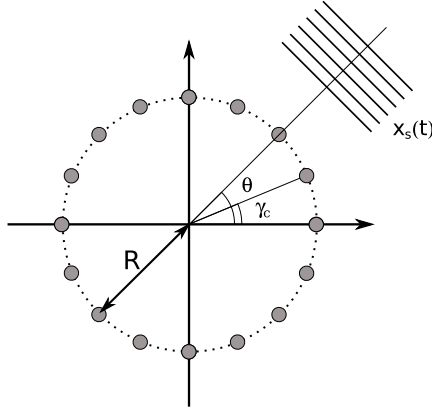


Figure 3.1: Incoming plane wave $x_s(t)$, on a uniform circular array.

3.2.2 Signal model

A broadband plane wave $x_s(t)$ impinging on the array is modeled in the frequency domain as

$$\mathbf{X}(\omega) = \mathbf{a}(\theta, k)X_s(\omega) + \mathbf{N}(\omega), \quad (3.2)$$

where $\mathbf{X}(\omega)$ is the output signal vector from the array, $\mathbf{a}(\theta, k)$ is the array manifold vector, $X_s(\omega)$ is the signal of interest, and $\mathbf{N}(\omega)$ is the combined noise and interference. The noise is assumed to be a spatially and temporarily uncorrelated Gaussian stochastic process. The interference consists of the contributions from other propagating modes and/or directions, that is, signals having different wavenumbers k and/or incident angles θ than the signal of interest.

Compared to bulk waves in isotropic solids, where there are only two modes of propagation, the boundary conditions of free thin plates create conditions for the existence of a class of guided waves called Lamb waves. Depending on the frequency of the received signal and the thickness of the plate, there are at least two possible propagation modes for every frequency, the symmetric mode S_0 and the asymmetric mode A_0 . As frequency is increased, the number of possible modes also increases. Lamb waves are dispersive in the sense that the phase velocity is frequency dependent. The possible modes for a given frequency-thickness product satisfy the so called Rayleigh-Lamb equations. Solving the Rayleigh-Lamb equations numerically allows the calculation of the phase velocity as a function of frequency for each mode, known as dispersion curves.

The wave propagation and excitation in a plate was modeled in two dimensions (see Figure (3.2)) using normal mode expansion.

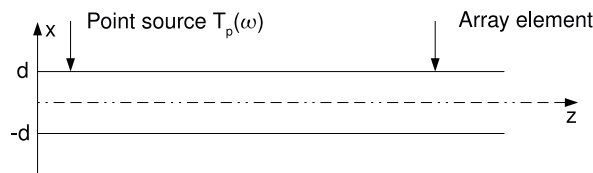


Figure 3.2: Illustration of the 2D-model showing the source and a receiving element on a plate having thickness $2d$.

The implementation was based on the work of Nunez [12]. The model assumes plane strain, which means that the strain in the y direction in Figure 3.2 is assumed to be zero. A traveling

harmonic Lamb wave mode n in the $+z$ direction having frequency ω is described by

$$U_i^{(n)}(x, z, \omega) = e^{jk_n(\omega)z} W_i^{(n)}(x, \omega), \quad (3.3)$$

where i is the displacement component (x or z). $W_k^{(n)}$ is the displacement amplitude and can be found in the literature, for example in [12]. The resulting displacement field is the sum of all modes

$$U_i(x, z, \omega) = \sum_n A_n(z, \omega) W_i^{(n)}(x, \omega), \quad (3.4)$$

where $A_n(z, \omega)$ is the amplitude and phase of mode n at z and frequency ω . The average power flow for mode n is

$$P_n(\omega) = \frac{1}{2} \omega^2 \rho V_G^{(n)}(\omega) \int_{-d}^d (|W_x^{(n)}(x, \omega)|^2 + |W_z^{(n)}(x, \omega)|^2) dx, \quad (3.5)$$

where $V_G^{(n)}$ is the group velocity of mode n . Using $P_n(\omega)$ and assuming a surface point source $T_p(\omega)$ at $z = p$ perpendicular to the plate, the amplitude of mode n is given by

$$A_n(z, \omega) = \frac{i\omega}{4P_n(\omega)} W_k^{(n)}(d, \omega) e^{jk_n(\omega)z} T_p(\omega) e^{-jk_n(\omega)(z-p)}. \quad (3.6)$$

3.2.3 Setup

To evaluate the proposed methods, a 15 mm thick aluminium plate was modeled. Two UCAs were used in the simulations, a 16 element and a 32 element array. Each element consists of a small diameter transducer, which is assumed to be a point-like receiver. The elements do not exhibit any load on the structure and they have a flat frequency response over the signal's frequency range. The incoming signal is generated by a point-like source normal to the surface of the plate. An illustration of the setup is presented in Figure 3.3.

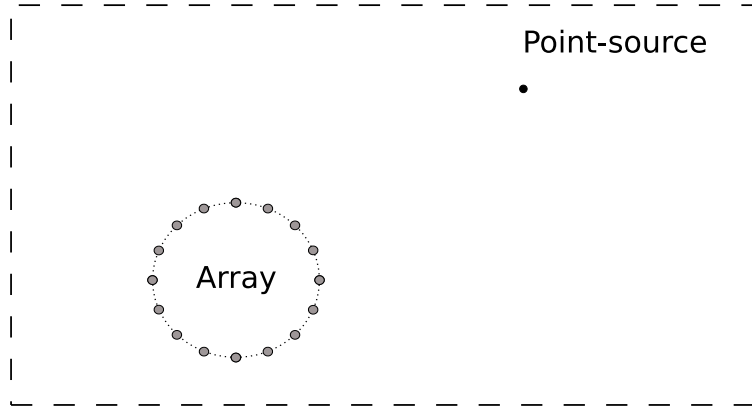


Figure 3.3: The array elements and the source are assumed to be point-like.

The resulting dispersion curves for the 15 mm aluminium plate are plotted in Figure 3.4.

3.3 Array processing of multimodal Lamb waves

3.3.1 Direction of Arrival Estimation

The main problem considered in this report, direction of arrival estimation, belongs to a general class of frequency-wavenumber $(\omega - \mathbf{k})$ estimation problems where the objective is to seek the

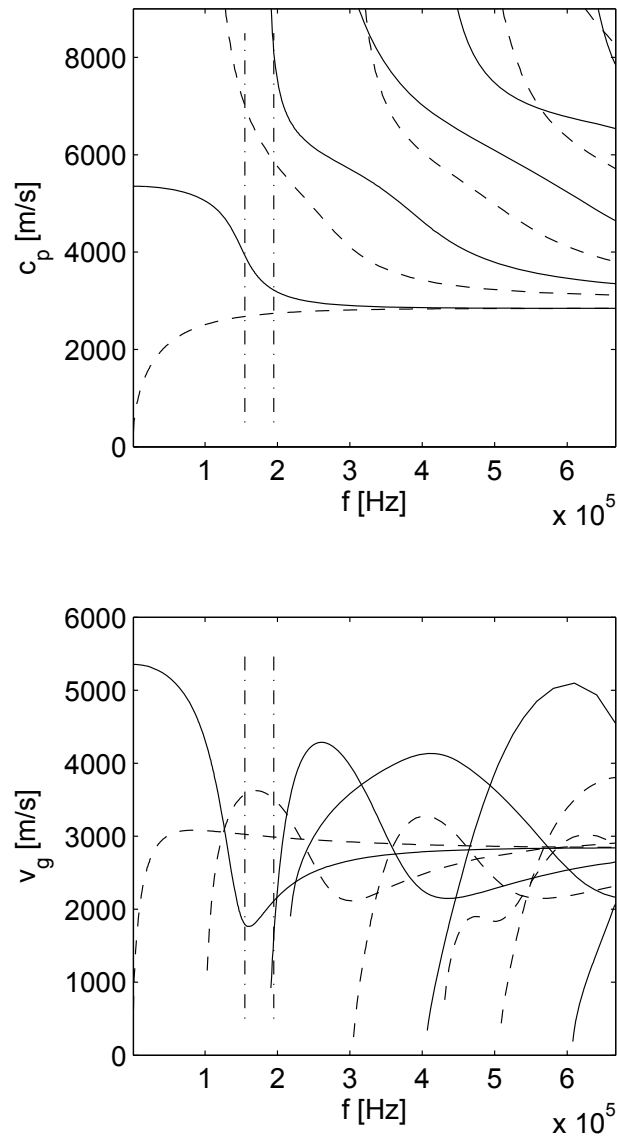


Figure 3.4: Phase velocity (top) and group velocity (bottom) dispersion curves of the 15 mm aluminium plate. Solid line - symmetric modes. Dashed line - asymmetric modes. Vertical lines show the frequency band of the signals used in the examples. Modes are numbered from left to right ($A_0, S_0, A_1, S_1 \dots$).

frequency-wavenumber amplitude spectrum, $P(\omega, \mathbf{k})$, of the incoming wave. The case of Lamb waves propagating in thin plates results in a two dimensional wavenumber domain. The presence of multiple wave modes at every given frequency, often encountered in the case of Lamb waves, complicates the DOA estimation problem. There is no obvious way to design a standard DAS beamformer that performs well in situations where the incoming wave at each frequency consists of significant components having different wavenumbers. This problem was addressed by Capon [13] in his pioneering work on high-resolution frequency-wavenumber estimation of seismic array data.

DOA estimation is a special case of frequency-wavenumber estimation where the incidence angle of the incoming signal is sought. This is done by expressing the two dimensional wavenumber in polar coordinates and performing a two dimensional search in $\theta - k$ using either the Capon or the MUSIC approach. The direction of arrival can then be found in the angular spectrum by summation over all k .

For the DAS beamformer direction of arrival estimation is performed by calculating the output power from the beamformer in all directions and determining the locations of significant peaks.

3.3.2 Beamformers

Phase Mode Excitation-based Beamformer

The most widely used technique for beamforming is the DAS beamformer. Its main advantages are robustness and simplicity. Its disadvantage is its low performance compared to more sophisticated techniques. DAS beamforming requires certain a priori information regarding the properties of the material, such as, wavenumber and phase velocity. This information is used to calculate an appropriate delay for each element in the array to steer the array in a desired direction. The result is a beamformer that maximizes the output power for signals with given wavenumber arriving from a certain direction.

Dispersive materials or wave types can also be handled if good estimates of wavenumber or phase velocity for each frequency are available. Single-mode signals are readily handled using this approach, while multi-mode signals are more complicated since at each frequency there are at least two possible modes characterized by different wavenumbers with unknown amplitudes. The performance of DAS beamformers expressed in terms of sidelobe level degrades severely if delay errors of multiple propagating wave modes are present.

The radiation power or amplitude response of a beamforming scheme expressed in function of azimuth is referred to as a beam pattern. Beam pattern design for an array generally involves a trade-off between a number of properties, e.g., the beam-width and the height of the first sidelobe. The beam-width determines the ability to dissolve two or more simultaneously incoming signals from closely spaced sources. The sidelobe level determines how much off-axis signals affect the output. For uniform linear arrays (ULAs) a standard way is to apply weights on individual array elements to achieve the desired beam pattern. Unfortunately, this methodology cannot be directly applied to UCAs. There exists, however, a very convenient and powerful approach to this problem. After transforming the array manifold into so called *beam space* representation, the beam pattern synthesis of the resulting virtual array manifold can be performed using the same techniques as for ULAs.

The basis for the beam space representation of UCAs is *phase mode excitation*, which is a way of describing the excitation of the array as a sum of phase modes. This representation is different from the *element space* representation used for ULAs, where the excitation is described by the contribution from each element individually. Details concerning phase mode beamformer

can be found in our previous report [9, 10].

Here, we only present the general signal flow of the phase mode UCA beamformer from the input signals at the array elements to its scalar output $y(i)$ (Figure 3.5). To determine the direction of arrival for incoming signals, the Butler matrix \mathbf{B}_{PM} is calculated for the angles of interest. The complex weighting vector \mathbf{w}_{PM} operating on the beamspace array manifold can be calculated using standard weighting (apodization) techniques. The scalar output $y(i)$ from the beamformer is calculated for each angle in order to find the azimuth of maximum power indicating the signal DOA.

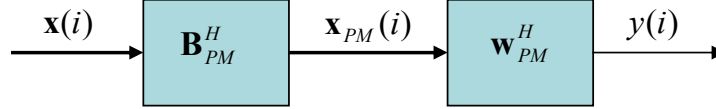


Figure 3.5: Scheme of a phase mode excitation beamformer. $\mathbf{x}(i)$ is the input signal, $\mathbf{x}_{PM}(i)$ is the input's beamspace representation, and $y(i)$ is the output from the beamformer.

Capon Beamformer

Compared to the data-independent DAS beamformers the data-dependent Capon beamformer has advantages that make it appropriate to use for Lamb wave detection and characterization. A Capon beamformer steered to a certain angle θ at wavenumber k adaptively attenuates noise and signals from other directions and wavenumbers. More formally, the Capon beamformer minimizes the mean output power from the array while passing signals from the steered direction and wavenumber undistorted. This can be expressed as [11]

$$\arg \min_{\mathbf{w}} \mathbf{w}^* \mathbf{S}_n(\omega) \mathbf{w} \quad \text{subject to } \mathbf{w}^* \mathbf{a}(\theta, k) = 1, \quad (3.7)$$

where \mathbf{w} is the array weighting vector, $\mathbf{a}(\theta, k)$ the array manifold vector and $\mathbf{S}_n(\omega)$ is the spectral density matrix of the noise and interferences in (3.2). The noise spectral density matrix is generally not known, instead the estimated data spectral density matrix $\mathbf{S}(\omega)$ is used. The solution to (3.7) subject to the constraints is

$$\mathbf{w}^* = \frac{\mathbf{a}(\theta, k)^* \mathbf{S}^{-1}(\omega)}{\mathbf{a}(\theta, k)^* \mathbf{S}^{-1}(\omega) \mathbf{a}(\theta, k)}. \quad (3.8)$$

The resulting output power from the beamformer is given by

$$\hat{P}(\omega, \theta, k) = \frac{1}{\mathbf{a}^*(\theta, k) \hat{\mathbf{S}}^{-1}(\omega) \mathbf{a}(\theta, k)}. \quad (3.9)$$

Denote the input signal from each array element m as $x_m(t)$. Each snapshot of $x_m(t)$ is segmented into N non-overlapping blocks. Performing a Fourier transform on each segment n results in $X_{n,m}(\omega)$. By forming $\mathbf{X}_n(\omega) = [X_{n,0}(\omega) X_{n,1}(\omega) \cdots X_{n,M}(\omega)]^T$, the spectral density matrix $\mathbf{S}(\omega)$ can then be estimated as

$$\hat{\mathbf{S}}(\omega) = \frac{1}{N} \sum_{n=1}^N \mathbf{X}_n(\omega) \mathbf{X}_n^*(\omega), \quad (3.10)$$

where N is the number of blocks that each snapshot is divided into. The estimated power of an incoming Lamb mode from angle θ with wavenumber $k_{mode}(\omega)$ is found by summation over all frequencies,

$$\hat{P}(\theta) = \sum_{\omega} \hat{P}(\omega, \theta, k_{mode}(\omega)). \quad (3.11)$$

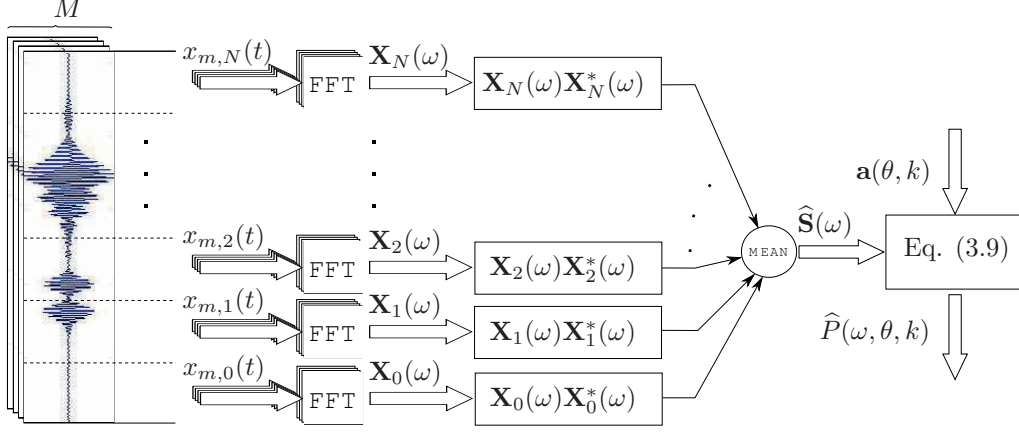


Figure 3.6: The flow chart shows the necessary steps for calculating the output power using the Capon beamformer for frequency ω , incident angle θ and wavenumber k . Selecting N and the length of the snapshot is a user design choice.

A flow chart of the Capon method is shown in Figure 3.6. For some applications it is of interest to estimate the frequency-wavenumber dispersion curves. This is straightforward by setting a fixed θ and calculating (3.9) for the range of frequencies and wavenumbers of interest. The last example in this report illustrates the result of such estimation.

The number of blocks N is a user design parameter which has to be chosen appropriately for each application. To obtain a non-singular $\hat{\mathbf{S}}(\omega)$ the number of blocks N has to be at least equal to the number of array elements M . This, however, does not guarantee that $\hat{\mathbf{S}}(\omega)$ is well-conditioned. Further increasing the number of blocks leads to reduced variance, but also reduces the resolution of the estimate. Increasing the length of the snapshot can compensate this, but it reduces the signal to interference plus noise ratio (SINR). A common way to handle these problems is to add a diagonal loading term, $\alpha \mathbf{I}$, to $\hat{\mathbf{S}}(\omega)$,

$$\hat{P}(\omega, \theta, k) = \frac{1}{\mathbf{a}^*(\theta, k) [\hat{\mathbf{S}}(\omega) + \alpha \mathbf{I}]^{-1} \mathbf{a}(\theta, k)}. \quad (3.12)$$

The diagonal loading increases the condition of the matrix. Selecting an appropriate value for α is also a user design choice. Setting α too low does not improve the condition of the matrix, setting α too high reduces the performance of the beamformer. One common way to set α is to make it proportional to the power of the received signal. For an in-depth analysis of diagonal loading see [14].

To reduce some of the effects from improper array element calibration, the signal coherence matrix \mathbf{C} can be used instead of \mathbf{S}

$$\hat{C}_{ij} = \frac{\hat{S}_{ij}}{\sqrt{\hat{S}_{ii} \hat{S}_{jj}}}. \quad (3.13)$$

Two essential disadvantages of the Capon beamformer are its disability to handle correlated signals and its limited robustness, which is lower than that of the DAS beamformer. The robustness can be improved by diagonal loading as mentioned above. Several different approaches to handle correlated signals have been presented in the literature, e.g., spatial smoothing [15] and the use of focusing matrices [16]. The authors are not aware of any attempts to use these techniques for Lamb waves.

3.3.3 Broadband MUSIC

The multiple signal classification (MUSIC) technique belongs to a class of techniques known as eigen-structure or sub-space based methods. These techniques are based on the principle of separation of eigenvector subspaces spanning the spatial covariance matrix or, more commonly used for broadband signals, the spectral density matrix. Eigen-structure analysis for DOA estimation of broadband signals can be performed on the narrowband components of the signal in the same way as presented in the previous section.

Here, we present different solution to the problem based on a broadband MUSIC algorithm, which was proposed by Wagner [17] for analyzing seismic signals from an array having an arbitrary geometry. Instead of working with the narrowband covariance matrix, in this approach a broadband spectral density matrix is formed with elements

$$\hat{S}_{ij} = \sum_{\omega} X_i(\omega)X_j^*(\omega), \quad (3.14)$$

where $X_i(\omega)$ and $X_j(\omega)$ are the FFTs of the signals received by array elements i and j , respectively. The next step is to calculate the eigenvalues and the eigenvectors of $\hat{\mathbf{S}}$ which are divided into two subsets in the following step. The first subset contains the largest eigenvalues whose corresponding eigenvectors will span the signal subspace. In the second subset the significantly smaller eigenvalues are included whose corresponding eigenvectors will span the noise subspace. The number of eigenvalues in the signal subspace will be equal to the number of received signals N_S . The number of signals that can be separated is less than the number of elements in the array. For narrowband single-mode signals, the incident angle θ can be determined through the standard MUSIC approach. This involves a search for mode vectors that are orthogonal to the noise eigenvectors. The mode vectors can be found by searching for the N_S highest peaks of the function

$$P_{pseudo}(\theta) = \frac{1}{\mathbf{a}^*(\theta)\mathbf{G}\mathbf{G}^*\mathbf{a}(\theta)}; \quad (3.15)$$

where $\mathbf{a}(\theta)$ is the array manifold vector and \mathbf{G} is a matrix consisting of the noise-subspace eigenvectors. $P_{pseudo}(\theta)$ can only be used to find the direction of an incoming signal, it is not a true power spectrum density and it is therefore often called a pseudo-spectrum.

To handle the multi-mode case with signals consisting of several components having different wavenumbers for each frequency, we consider mode vectors as functions of two arguments, θ and k , where k is the wavenumber. This approach overcomes the problems associated with dispersion, and in particular, the problem with multi-mode signals having different dispersion curves. It is also computationally convenient that only one eigendecomposition needs to be performed. The signal mode vector search now needs to be performed in two dimensions,

$$P_{pseudo}(\theta, k) = \frac{1}{\mathbf{a}^*(\theta, k)\mathbf{G}\mathbf{G}^*\mathbf{a}(\theta, k)}. \quad (3.16)$$

The signal flow of the MUSIC algorithm is presented in Figure 3.7.

The incident angles can then be found by summation over k . Similarly to the Capon method, the standard MUSIC technique is unable to handle correlated signals. Another limitation is that the number of signals has to be less than the number of elements.

3.4 Simulation results

In this section we present selected simulated results comparing the performance of the three techniques under various conditions. The simulated signals were generated using the technique presented in Section 3.2.2.

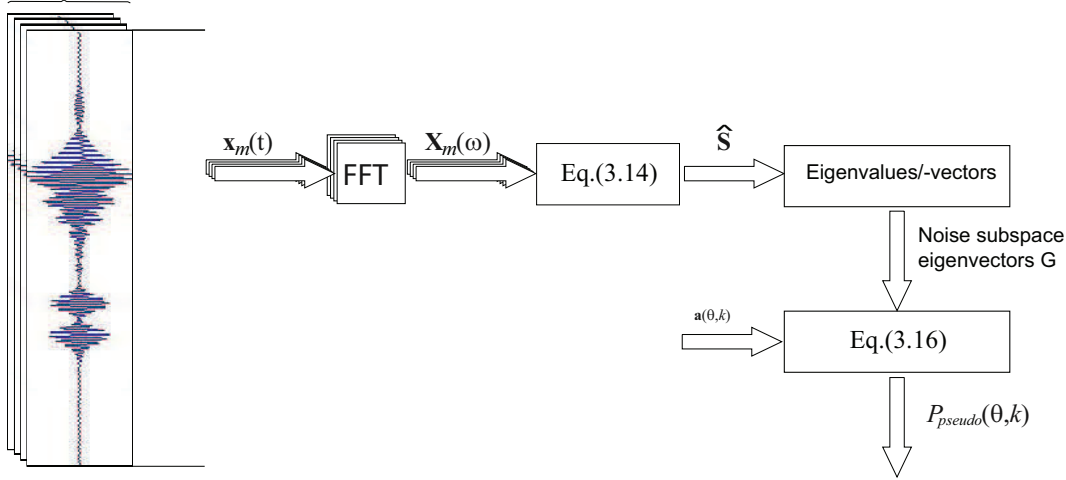


Figure 3.7: The flow chart shows the MUSIC algorithm step-by-step.

A bandpass filtered uncorrelated additive Gaussian white noise was added to each channel.

We start from comparing the performance of a 16 element UCA for different incoming signals. Figure 3.8 shows the performance of the algorithms for a single S_0 signal. The DAS beamformer performs as expected for this case where the phase velocity is set to the correct value for the S_0 mode.

Figures 3.9 and 3.10 show two signals, one having a clear separation between the S_0 , A_0 and A_1 modes, and the other with the A_0 and A_1 modes overlapping. The beampatterns produced by the algorithms for the two cases are shown in the lower plot of each figure. In this case where the signal is composed of three modes, the sidelobes of the DAS beamformer become higher.

In Figure 3.11 the resolving abilities of the algorithms are compared. Two S_0 - A_0 - A_1 signals arriving simultaneously to the array from different angles (0° and -34°) were simulated. Again the high-resolution techniques are able to separate the signals, while the DAS beamformer fails to make a separation.

Figure 3.12 show an example of using Capon's technique for Lamb wave characterization. The input signal consists of 2.3 ms of white noise bandpass filtered to 200 - 1200 kHz. The resulting A_0 - S_0 mode signal is received by a 32 element array from a predetermined angle. A clear separation of the two modes can be seen and the frequency-wavenumber estimates from the noisy measurement agree well with the true values.

3.5 Discussion and conclusions

Algorithms for direction of arrival estimation of multi-modal Lamb waves using UCAs were considered in the report. Three techniques for array processing have been evaluated, the UCA DAS beamformer, and the high resolution Capon and MUSIC algorithms. It was explained why the standard beampattern design techniques operating in element space, commonly used for uniform linear arrays are not directly applicable for UCAs.

It was shown how UCA DAS beamformers can be designed using techniques operating in beamspace. However, when steering the DAS beamformer in a desired direction, it is necessary to choose for which particular Lamb mode the beamformer delays will be calculated for. Other Lamb modes impinging from the same direction will not add up coherently but will result in increased sidelobes that reduce the performance of the beamformer.

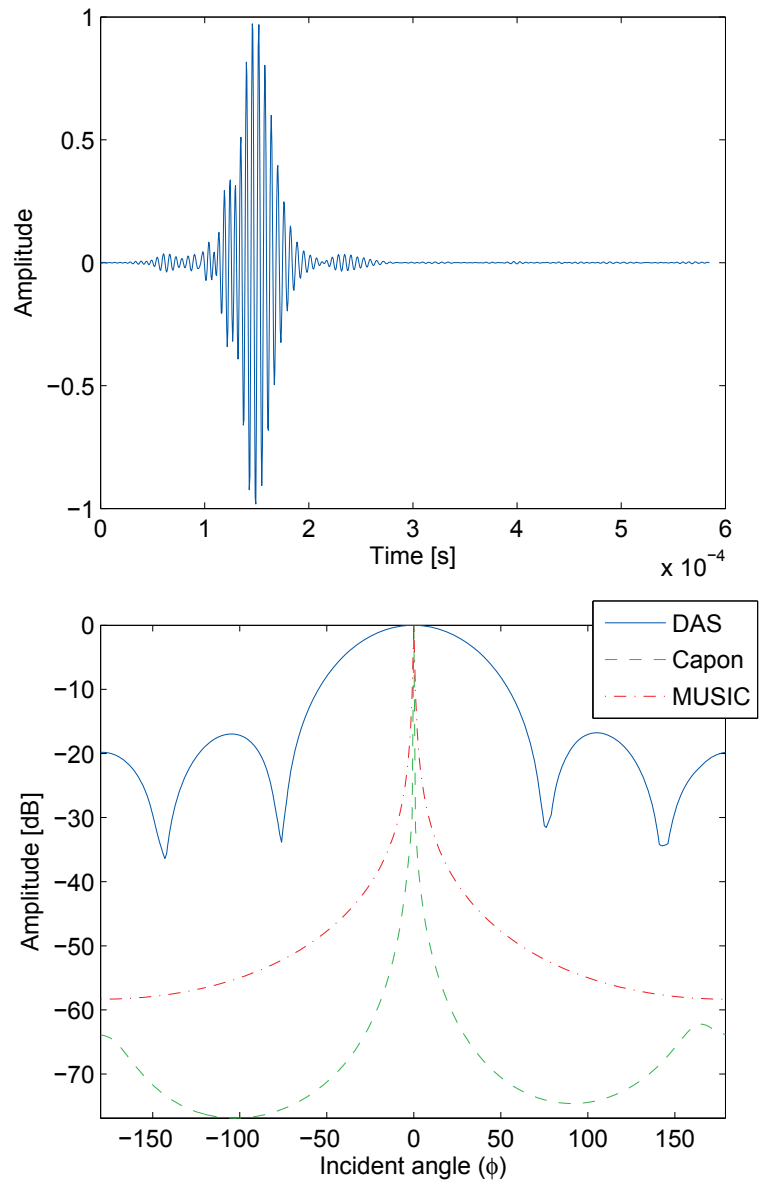


Figure 3.8: Single mode S_0 .

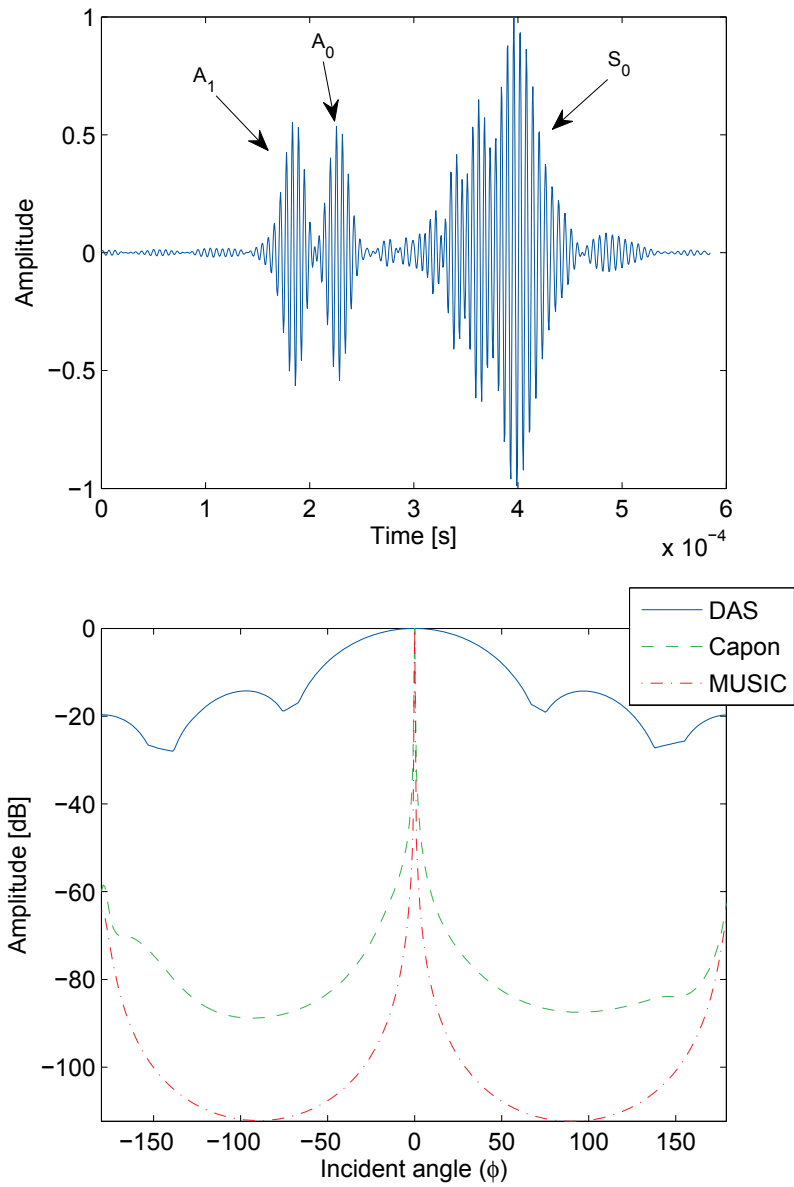


Figure 3.9: Signal and beam pattern for three mode signal. Top figure show received signal from a source 0.8 m from the array. Bottom figure shows corresponding beam patterns.

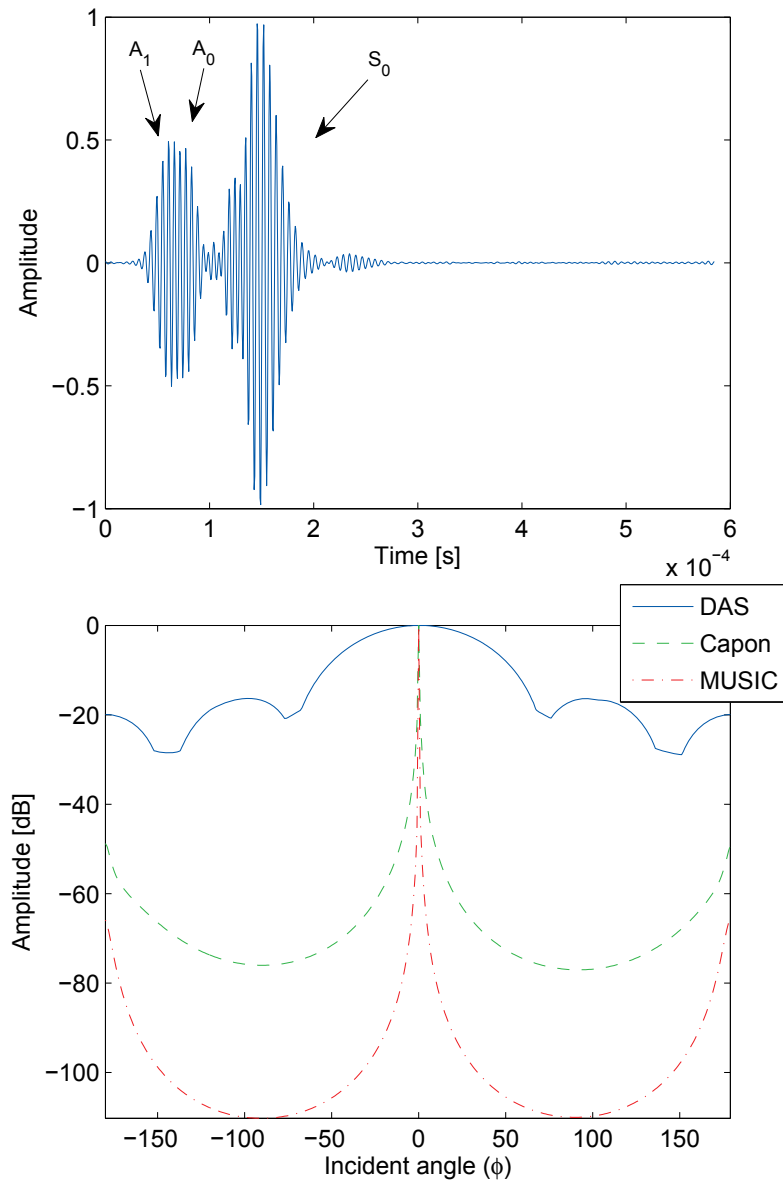


Figure 3.10: Signal and beampattern for three mode signal. Top figure show received signal from a source 0.35 m from the array. Bottom figure shows corresponding beampatterns.

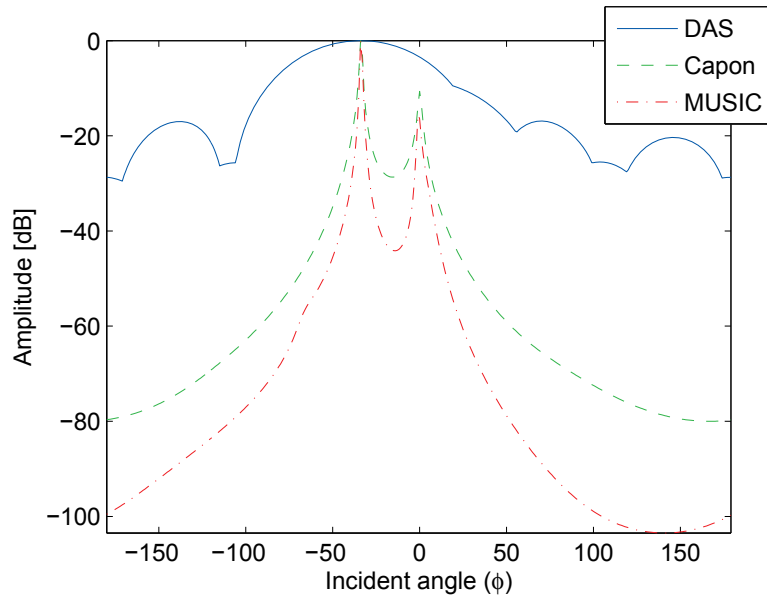


Figure 3.11: Resolving abilities for the different algorithms for two multimode incoming signals from incident angles 0° and -34° .

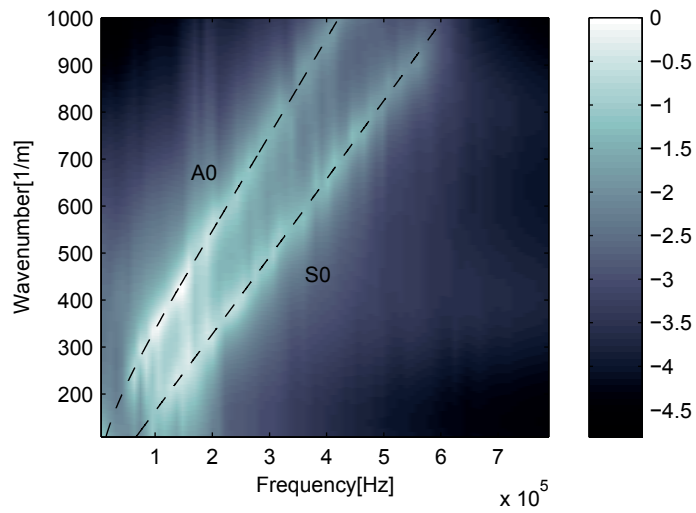


Figure 3.12: Capon frequency-wavenumber estimate of incoming signal under noise for a 5 mm thick Al-plate. Solid lines show the true wavenumbers for the A_0 and the S_0 mode respectively.

The Capon beamformer handles this in a more sophisticated way by adaptively setting the beamformer's weights to attenuate the other modes. MUSIC represents another approach, which is based on searching for vectors orthogonal to the noise subspace. The MUSIC technique has potentially higher resolution than Capon for DOA estimation.

The simulations presented in the report have shown, as expected, that the high-resolution methods (Capon and MUSIC) outperform the DAS beamformer, especially for multi-mode signals. The high-resolution methods are also superior when it comes to source separation. The Capon frequency-wavenumber estimation technique has been shown to be a very flexible and powerful approach for Lamb wave characterization, especially since it can be used for any array geometry. MUSIC performs even better than Capon but it is only capable of detecting the presence of a signal arriving from a certain direction with certain wavenumber. Unlike Capon, MUSIC cannot be used to calculate an array weighting vector based on the data. Its other drawback is the need to determine the size of the noise subspace, that is, the number of signal sources. MUSIC can only handle cases when the number of signals is less than the number of array elements. A common disadvantage of both high-resolution techniques is their difficulty in handling correlated signals.

Bibliography

- [1] V. Giurgiutiu and J. Bao. Embedded-ultrasonics structural radar for in situ structural health monitoring of thin-wall structure. *Structural Health Monitoring*, 3(2):121–140, 2004.
- [2] S. Sundararaman, D. E. Adams, and E. J. Rigas. Structural damage identification in homogeneous and heterogeneous structures using beamforming. *Structural Health Monitoring*, 4(2):171–90, 2005.
- [3] V. Giurgiutiu. *Structural Health Monitoring with Piezoelectric Wafer Active Sensors*. Academic Press, 2008.
- [4] P.D. Wilcox, P. Cawley, and M.J.S. Lowe. Acoustic fields from PVDF interdigital transducers. *IEE Proceedings-Science, Measurement and Technology*, 145(5):250 – 9, 1998.
- [5] P.D. Wilcox, M.J.S. Lowe, and P. Cawley. Lamb and SH wave transducer arrays for the inspection of large areas of thick plates. In *Annual Review of Progress in QNDE*, volume 19A, pages 1049 – 56, 2000.
- [6] P.D. Wilcox. Omni-directional guided wave transducer arrays for the rapid inspection of large areas of plate structures. *IEEE Transactions on Ultrasonics, Ferroelectrics and Frequency Control*, 50(6):699 – 09, 2003.
- [7] A. Velichko and P.D. Wilcox. Guided wave arrays for high resolution inspection. *Journal of the Acoustical Society of America*, 123(1):186 – 96, 2008.
- [8] P. Fromme, P.D. Wilcox, M.J.S. Lowe, and P. Cawley. On the development and testing of a guided ultrasonic wave array for structural integrity monitoring. *IEEE Transactions on Ultrasonics, Ferroelectrics and Frequency Control*, 53(4):777 – 85, 2006.
- [9] T. Stepinski (editor), T. Olofsson, and E. Wennerström. Inspection of copper canisters for spent nuclear fuel by means of ultrasound - ultrasonic imaging, FSW monitoring with acoustic emission. Technical Report TR-06-47, SKB, 2006.

- [10] T. Stepinski (editor), M. Engholm, and T. Olofsson. Inspection of copper canisters for spent nuclear fuel by means of ultrasound - FSW monitoring with acoustic emission, copper characterization and ultrasonic imaging. Technical Report TR-08-12, SKB, 2008.
- [11] H. L. Van Trees. *Optimum Array Processing*, volume 4 of *Detection, Estimation, and Modulation Theory*. Wiley-Interscience, 2002.
- [12] I. Nunez, R.K. Ing, C. Negreira, and M. Fink. Transfer and green functions based on modal analysis for lamb waves generation. *Journal of the Acoustical Society of America*, 107(5):2370 – 8, 2000.
- [13] J. Capon. High-resolution frequency-wavenumber spectrum analysis. *Proceedings of the IEEE*, 57(8):1408 – 18, 1969.
- [14] J. Li, P. Stoica, and Z. Wang. On robust capon beamforming and diagonal loading. *IEEE Transactions on Signal Processing*, 51(7):1702 – 15, 2003.
- [15] T.-J. Shan, M. Wax, and T. Kailath. On spatial smoothing for direction-of-arrival estimation of coherent signals. *IEEE Transactions on Acoustics, Speech, and Signal Processing*, ASSP-33(4):806 – 11, 1985.
- [16] H. Hung and M. Kaveh. Focussing matrices for coherent signal-subspace processing. *IEEE Transactions on Acoustics, Speech, and Signal Processing*, 36(8):1272 – 81, 1988.
- [17] G.S. Wagner and T.J. Owens. Broadband eigen-analysis for three-component seismic array data. *IEEE Transactions on Signal Processing*, 43(7):1738 – 41, 1995.

Chapter 4

Efficient Algorithms for Synthetic Aperture Imaging

by Tomas Olofsson

4.1 Introduction

The immersion setup is often used for ultrasonic imaging in nondestructive testing (NDT) due to its advantages compared to contact measurements. Most importantly, the presence of the water sound path provides more repeatable inspection conditions compared to contact testing since much of the problems with poor and varying acoustic coupling between transducer and test object due to, e.g. rough surfaces can be avoided. On the other hand, the use of immersion testing causes some problems in the data processing that are not present, or not as pronounced, when contact testing is used.

In the contact testing, the synthetic aperture focusing technique (SAFT) can be used quite straightforwardly to reconstruct high resolution images from the acquired data provided that the test object is isotropic and homogenous. SAFT is the ultrasonic counterpart to synthetic aperture radar (SAR) [1] and the idea in both SAR and SAFT is to scan a sensor to acquire measurements from several points along a line and post-process the obtained signals in a way that mimics the behavior of a lens. The most essential difference between SAFT and lens (or a phased array) is that in SAFT each point in a region of interest is treated using an individual focal law. The synthetic aperture that is created is larger than the aperture of the individual sensors and, as a consequence, the lateral resolution of the images obtained in this way is far better than the resolution in the raw data.

SAR and SAFT can be implemented either in the space-time domain using the *delay-and-sum* (DAS) technique or in the wave number-frequency domain, often referred to as the $\omega - k$ method. In the limit if no approximation is used, both processing techniques would yield the same results. The main benefit of working in the frequency domain is the improved computational efficiency. Frequency domain implementations have been widely used in SAR since the 80'th whereas in NDT, the use of DAS is still the dominant implementation. Few exceptions of the use of the $\omega - k$ method in NDT were presented, [2–5].

Unfortunately, ultrasonic data acquired using immersion testing is not ideally suited for SAFT processing. The difficulty is caused by the refraction at the interface between water and test object since the time delays that are necessary for DAS are more difficult to compute when refraction is present.¹ Furthermore, the conventional $\omega - k$ methods are based on a constant wave velocity and therefore the conventional frequency domain algorithms do not provide a solution to the problem either.

A scenario with several layers having different sound velocities is an often occurring condition in reflection seismology which aims at estimating the properties of the Earth's subsurface using pulse-echo measurements. In seismology, an approach that is strongly related but not equivalent to SAR and SAFT, called *migration*, has been developed, [6]. Unlike SAR and SAFT, migration makes explicit use of the wave equation in the processing. Viewing the measured signals at the sensors as a boundary condition for the wave equation, the field can be extrapolated both forward and backward in time and space. By essentially "turning the clock back", the field is back-tracked to the source points.

The early implementations of migration used numerical finite difference algorithms [7], followed later by Fourier transform based methods [8]. The phase shift migration method reported in [9] presented a frequency domain solution for media that are homogenous in the lateral direction but inhomogeneous in depth. The approach presented in [9] has recently been used in ground penetrating radar (GPR) [10] in which the problem of having different wave propagation in air and soil must be treated and for which the conventional SAR methods thus are inadequate.

¹For instance, finding the propagation time between two points separated by one interface involves solving a fourth order equation.

In this work we investigate phase shift migration for imaging data acquired using immersion testing. The considered application is immersion testing of copper blocks and the experiments aim at demonstrating the potential of phase shift migration for this application.

The theory and the algorithm are given in the section below. The experiments are presented in Section 4.3 and, finally, conclusions and a discussion are given in Section 4.4

4.2 Theory

In this section we give a derivation of the reconstruction algorithm used in the work. The presentation is based on that presented in [10] and the derivation presented in Section 4.2.1 is made for a scenario where the inspected object consists of a number of sources that "explode" at time $t = 0$, creating a field that is simultaneously measured using an array of sensors. This description is not valid for the single transducer scanned pulse-echo measurements, which we hereafter call the monostatic case², and in Section 4.2.2 it is described how the derived method can be adapted to the monostatic case. A summary of the algorithm is given in Section 4.2.3. Additionally, some comments on the aliasing problem that is associated with the use of discrete data and the discrete Fourier transform are given in Appendix.

4.2.1 Phase shift migration for the "exploding source" scenario

Phase-shift migration for a 2D-scenario starts out from the 2D scalar wave equation which holds with good approximation for longitudinal waves. We here consider propagation in the xz -plane, thus assuming the field to be independent of y , see Figure 4.1 for a definition of the coordinate system. Let $p(x, z, t)$ denote the field at coordinate (x, z) at time t . The 2D scalar equation wave equation states that

$$\left[\frac{\partial^2}{\partial x^2} + \frac{\partial^2}{\partial z^2} - \frac{1}{c^2} \frac{\partial^2}{\partial t^2} \right] p(x, z, t) = 0, \quad (4.1)$$

where c is the velocity.

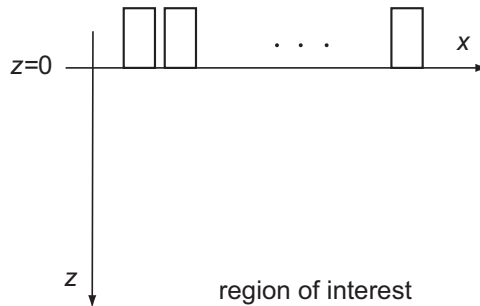


Figure 4.1: The coordinate system used in the derivation of the phase shift migration method. The field is assumed to be measured simultaneously using an array of closely spaced sensors at depth $z = 0$ along the x -axis.

By taking the Fourier transform over x , z , and t , we obtain

$$\left(-k_x^2 - k_z^2 + \frac{\omega^2}{c^2} \right) P(k_x, k_z, \omega) = 0, \quad (4.2)$$

²The term "monostatic" is borrowed from the radar community

where k_x and k_z are components of the wave number vector and ω is the angular frequency.

We are interested in a non-trivial solution where $P(k_x, k_z, \omega) \neq 0$ and this means that the *dispersion relation*

$$k_x^2 + k_z^2 = \frac{\omega^2}{c^2} \quad (4.3)$$

must be fulfilled, from which we can get k_z

$$k_z = \pm \sqrt{\frac{\omega^2}{c^2} - k_x^2}. \quad (4.4)$$

If we transform eq. (4.1) over t and x we get

$$\left[-k_x^2 + \frac{\partial^2}{\partial z^2} + \frac{\omega^2}{c^2} \right] P(k_x, z, \omega) = 0. \quad (4.5)$$

By combining (4.3) and (4.2) we obtain the ordinary differential equation

$$\left[\frac{\partial^2}{\partial z^2} + k_z^2 \right] P(k_x, z, \omega) = 0, \quad (4.6)$$

which has the solution

$$P(k_x, z, \omega) = A e^{\pm j k_z z}, \quad (4.7)$$

where A is constant that is determined from the boundary conditions for the solution. Those boundary condition consist of the measurements that are performed at $z = 0$, which means that we know $P(k_x, z = 0, \omega)$.

By appropriate choices of the signs in eqs. (4.7) and (4.4), in combination with the consideration of solutions with negative ω only, we can obtain a solution in which only the up-going (negative z -axis) waves are considered. Altogether this yields the solution

$$P(k_x, z, \omega) = \begin{cases} P(k_x, z = 0, \omega) \exp\{j \sqrt{\frac{\omega^2}{c^2} - k_x^2} z\} & \text{for } \omega < 0 \\ 0 & \text{otherwise} \end{cases}. \quad (4.8)$$

The operation in (4.8) represents a phase shift and from this relation *phase shift migration* has got its name.

Eq. (4.8) describes the relation between the field measured at $z = 0$ and the field that would have been measured at $z \neq 0$ if the sensors had been placed at that particular depth instead of $z = 0$. By taking the inverse Fourier transform of $P(k_x, z, \omega)$ with respect to k_x and ω we can recover $p(x, z, t)$.

Consider now a source located at the particular depth, z . Since the distance between the hypothetical sensor plane and the source in such case is zero, the contribution from the source will appear at $t = 0$. Moreover, compared to any other observation times, the field originating from the source will be maximally concentrated in space at $t = 0$. We realize that by simply reading out the field at time $t = 0$ from $p(x, z, t = 0)$ for all points at the same depth, z , we will get an image line that has optimal lateral resolution. Time $t = 0$ is sometimes called the *imaging condition* for this scenario.

The inverse Fourier transform for obtaining $p(x, z, t = 0)$ is

$$p(x, z, t = 0) = \int \int P(k_x, z, \omega) e^{j k_x x} dk_x d\omega = \int \left[\int P(k_x, z, \omega) d\omega \right] e^{j k_x x} dk_x, \quad (4.9)$$

where we have used that $e^{j\omega t} = 1$ for $t = 0$. The last expression points out that the computations can be performed by integration of $P(k_x, z, \omega)$ over ω , followed by an inverse 1D Fourier transform over k_x .

Note further that if c is constant throughout the inspected volume, we can directly extrapolate the field at any given depth using the expression in (4.8). The situation is more complicated when the velocity is varying within the volume. One situation that, however, can be relatively easily treated is when the velocity varies only with z . In particular, let us consider a situation with a layered structure consisting of L layers, each having a constant sound velocity, i.e.

$$c(z) = \begin{cases} c_0 & \text{for } z \in [0, z_0] \\ c_1 & \text{for } z \in (z_0, z_1] \\ \vdots & \\ c_L & \text{for } z \in (z_{L-1}, z_L] \end{cases} \quad (4.10)$$

For this situation we can easily find the general solution by viewing the solution at a layer interface as the boundary condition for a subsequent downward extrapolation for z . For z belonging to the l :th layer, this approach yields the solution

$$P(k_x, z, \omega) = P(k_x, z = 0, \omega) \exp \left\{ j \left(\left(\sum_{m=0}^{l-1} \sqrt{\frac{\omega^2}{c_m^2} - k_x^2} \Delta_m \right) + \sqrt{\frac{\omega^2}{c_l^2} - k_x^2} (z - z_{m-1}) \right) \right\}, \quad (4.11)$$

where Δ_m is the thickness of the m :th layer.

Finally, note that the solution for $P(k_x, z, \omega)$ can be calculated recursively. If we have $P(k_x, z, \omega)$, we can obtain $P(k_x, z + \Delta z, \omega)$ with z and $z + \Delta z$ both being within the same layer, l , using

$$P(k_x, z + \Delta z, \omega) = P(k_x, z, \omega) \exp \left\{ j \sqrt{\frac{\omega^2}{c_l^2} - k_x^2} \Delta z \right\}. \quad (4.12)$$

If we choose a regular image grid in z , the factor $\exp \left\{ j \sqrt{\frac{\omega^2}{c_l^2} - k_x^2} \Delta z \right\}$ will be the same for each image line within that layer meaning that the factor can be pre-calculated and stored in a lookup table to speed up the computations.

4.2.2 Adaptations to the case of pulse-echo measurements.

As noted earlier, there is a discrepancy between the assumptions leading to the phase shift migration equations and the assumptions that are valid for the monostatic case. Since the actual measurements are performed in pulse-echo mode, all sound paths are twice as long as those considered in the exploding source scenario and a simple way of handling this is to translate the pulse-echo scenario to an analogous exploding source case having exactly half the velocity as the physical pulse-echo setup.

By replacing c with $c/2$ in eq. (4.8), we obtain the basic relation

$$P(k_x, z, \omega) = P(k_x, z = 0, \omega) \exp \left\{ j \sqrt{\frac{4\omega^2}{c^2} - k_x^2} z \right\}, \quad (4.13)$$

and the expressions in eqs. (4.11) and (4.12) should be adapted in the same way.

Another deviation from the above presented theory is that the field measurements are influenced by the transducer characteristics. The electro-acoustical properties of the transducer

affect the measured signal both at transmission and reception and the overall effect is that the received signals become band-pass filtered and, more importantly, phase delayed. If these delays are not compensated for, the imaging condition $t = 0$ will be poorly synchronized with the waves arriving from a scatter at z , which causes a deterioration of the lateral resolution.

A simple and robust technique to compensate for the phase delays caused by the transducer is to apply a matched filter to the measured signal prior to the migration. This is conveniently done in the frequency domain for each acquired signal, $s(x_n, z = 0, t)$, as

$$P_{MF}(x_n, z = 0, \omega) = S(x_n, z = 0, \omega)H^*(\omega) \quad (4.14)$$

where $S(x_n, z = 0, \omega)$ is the Fourier transform of $s(x_n, z = 0, \omega)$ and $H(\omega)$ is the transfer function describing the combined filtering effect from the transducer, both in transmission and reception. The impulse response corresponding to $H(\omega)$ can be easily measured as the response from a reflector in the far field.

4.2.3 Summary of the algorithm

The algorithm summarized in this section aims at reconstructing an image of size $M \times N$ where M and N are the number of image lines in the z - and x directions, respectively. M is arbitrary and the lines are separated by a distance Δz . The N image lines parallel to the z -axis are separated by the spatial sampling distance Δx .

Let $s(x_n, z = 0, t)$ denote the signal acquired at the transducer position x_n . The migration algorithm proposed here can be summarized as follows:

1. For $n = 1, \dots, N$, compute the Fourier transform of $s(x_n, z = 0, t)$:

$$S(x_n, z = 0, \omega) = \int s(x_n, z_0 = 0, t)e^{-j\omega t} dt \quad (4.15)$$

2. For $n = 1, \dots, N$, perform matched filtering combined with nulling out Fourier coefficients corresponding to waves traveling downwards:

$$P(x_n, z = 0, \omega) = \begin{cases} S(x_n, z_0 = 0, \omega)H^*(\omega) & \text{if } \omega < 0 \\ 0 & \text{otherwise} \end{cases} \quad (4.16)$$

3. Zero-pad $P(x_n, z = 0, \omega)$ in the x -direction as

$$P_{zp}(x_n, z = 0, \omega) = \begin{cases} P(x_n, z = 0, \omega) & \text{for } n \in [1, N] \\ 0 & \text{for } N + 1 \leq n \leq N + N_x \end{cases} \quad (4.17)$$

where the number of padded zeros, N_x is chosen according the guidelines given in the Appendix. Fourier transform the zero-padded data with respect to x :

$$P(k_x, z = 0, \omega) = \int P_{zp}(x, z_0 = 0, \omega)e^{-jk_x x} dx. \quad (4.18)$$

As noted below, the integrals are in practice replaced by sums and for the above integral, the sum runs over x_n .

4. Set $z_0 = 0$ and iterate (a) and (b) below for $m = 0, \dots, M - 1$.

- (a) Use the phase-shift relation to compute $P(k_x, z_{m+1} = z_m + \Delta z, \omega)$:

$$P(k_x, z_{m+1} = z_m + \Delta z, \omega) = P(k_x, z_m, \omega) \exp\left(j\sqrt{\frac{4\omega^2}{c_l^2} - k_x^2}\Delta z\right), \quad (4.19)$$

where c_l is sound velocity in the considered layer.

- (b) Compute the field $p(x, z_{m+1}, t = 0)$ by the inverse Fourier transform at the imaging condition $t = 0$

$$p(x, z_{m+1}, t = 0) = \int \int P(k_x, z_{m+1}, \omega) e^{jk_x x} dk_x d\omega \quad (4.20)$$

and assign $p(x, z_{m+1}, t = 0)$ to be the m :th image line.

Please note that all involved Fourier transforms are in practice computed using the fast Fourier transform. See Appendix for comments on aliasing problem that occurs when when continuous data is replaced with sampled values.

4.3 Experiments

Two experiments were performed. The first aimed at demonstrating the method's ability to treat a scenario with two scatterers residing in layers having different velocity. This experiment, which is presented in Section 4.3.1, was performed with a copper block immersed in water and containing a number of side drilled holes. A wire target was placed in front of the block in water. In this way we created a scenario with scatterers present both in the slow water media and in the fast copper media. The second experiment aimed at demonstrating how the method improves the resolution in C-scans and at the same time suppresses grain noise. The test object in this experiment that is presented in Section 4.3.2 was a copper block with flat bottom holes.

4.3.1 Immersion test of copper block with side drilled holes and wire target

The immersion test setup used in the experiments is shown in Fig. 4.2. A 2.25 MHz planar circular transducer from Panametrics with 10 mm diameter was scanned along the x -axis and pulse-echo measurements were acquired at positions x_1, \dots, x_{210} that were separated by $\Delta x = 1$ mm. The inspected object was placed with its front surface in the horizontal plane.

In Figure 4.4 the image obtained by phase shift migration is presented. In the migrated image, the responses from the SDHs are concentrated to small spots and the same holds for the wire target. Note that an automatic geometrical correction is obtained through the migration since the method takes into account the different velocities at different layers. For example, the wire target's distance between to the front surface of the block can be correctly measured in the image to be 7 mm. Note also that the lateral resolution of the SDHs are approximately equal throughout the entire object.

The diffuse spot centered at $x = 110$ mm and $z = 61$ mm corresponds the above mentioned double reflection Cu-wire-Cu. Since multiple reflections are not taken into account in the development of the method, such echoes generally lead to blurred artifacts as the one seen here.

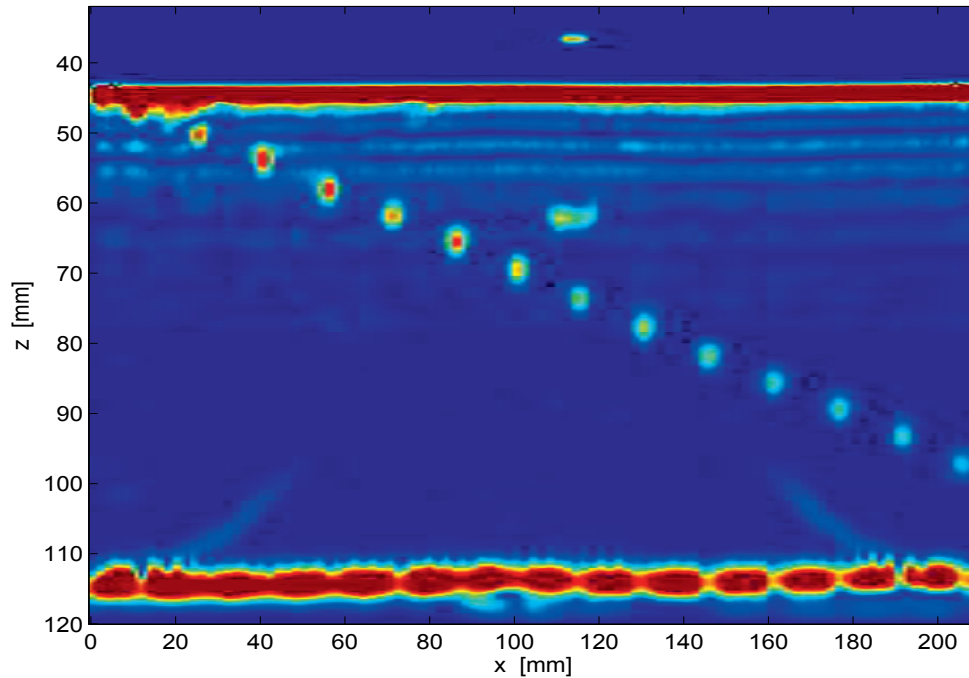


Figure 4.4: Image obtained by phase shift migration. The hyperbolic patterns representing the SDHs as well as the wire target have been transformed to small spots with lateral resolution that is approximately independent of depth.

The lateral resolution can be further examined in Figure 4.5, where local profile plots for each SDH are shown both for the B-scan and the reconstructed image. These profiles were obtained by calculating the maximum amplitudes within a depth interval covering each hole and projecting the values onto the x -axis. For instance, the profile of the SDH at $x = 100$ was obtained using data in the rectangle defined by $x \in [93, 107]$ mm and $z \in [82, 84]$ mm. For ease of comparison, the cross sections have been normalized to have the same maximum amplitudes.

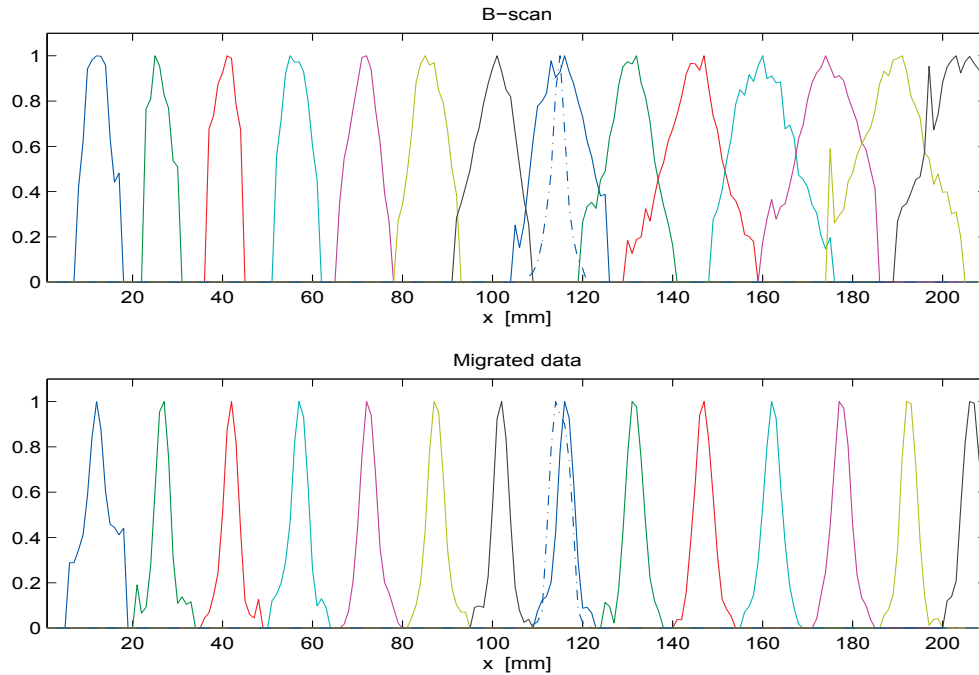


Figure 4.5: Profile plot of the SDHs and the wire target in the original B-scan (upper) and the reconstructed image (lower). The profiles of SDHs are shown as solid lines and the profile of the wire target is dash-dotted.

Inspection of the profiles shown in Figure 4.5 confirms the conclusion that the lateral resolution in the reconstructed image is practically independent of the depth. This holds also for the wire target which is surrounded by a medium with a different sound velocity than the SDHs.

4.3.2 Immersion test of copper block with flat bottom holes

In the second experiment we performed a volume scan of a copper block with flat bottom holes (FBHs) located close to its bottom. The dimension of the block are shown in Figure 4.6. The purpose of the experiment was to illustrate the improvements in detectability and lateral resolution that can be achieved through the method. The block has a grainy structure that causes both grain noise and sound attenuation causing the responses of the FBHs to be relatively difficult to detect in standard B-scans. Only the 4 mm diameter FBH gives a response that is easily detected in those images.

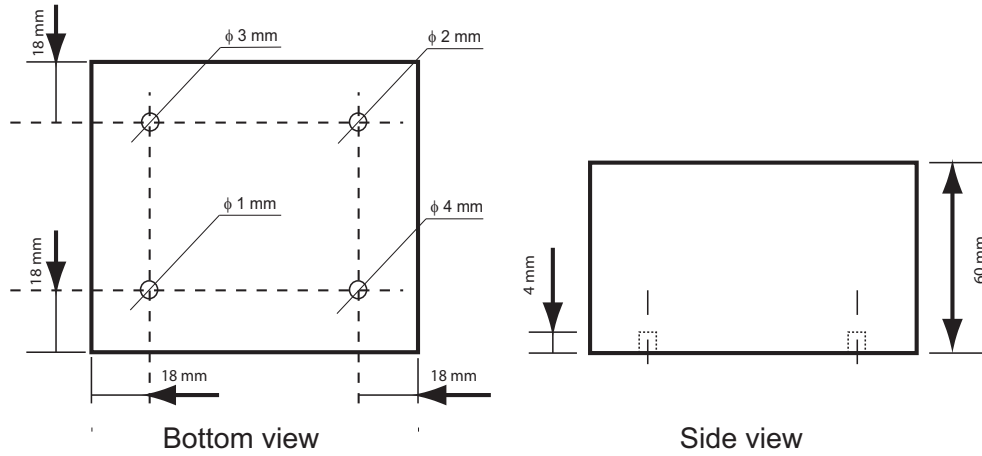


Figure 4.6: Copper block with four FBHs.

Figures 4.7 and 4.8 show two example of an envelope B-scans from the data set. The first shows a cross section over the 1 mm and 4 mm FBHs. The 1 mm hole is not seen at all but the response from the 4 mm FBH can be seen at $x = 82$ mm and $t \approx 82\mu s$. Note that the width of the response is approximately 15 mm. Figure 4.8 shows a cross section over 2 mm and 3 mm and we can see weak responses from these holes at $t \approx 82\mu s$, at $x \approx 18$ mm and $x \approx 80$ mm, respectively.

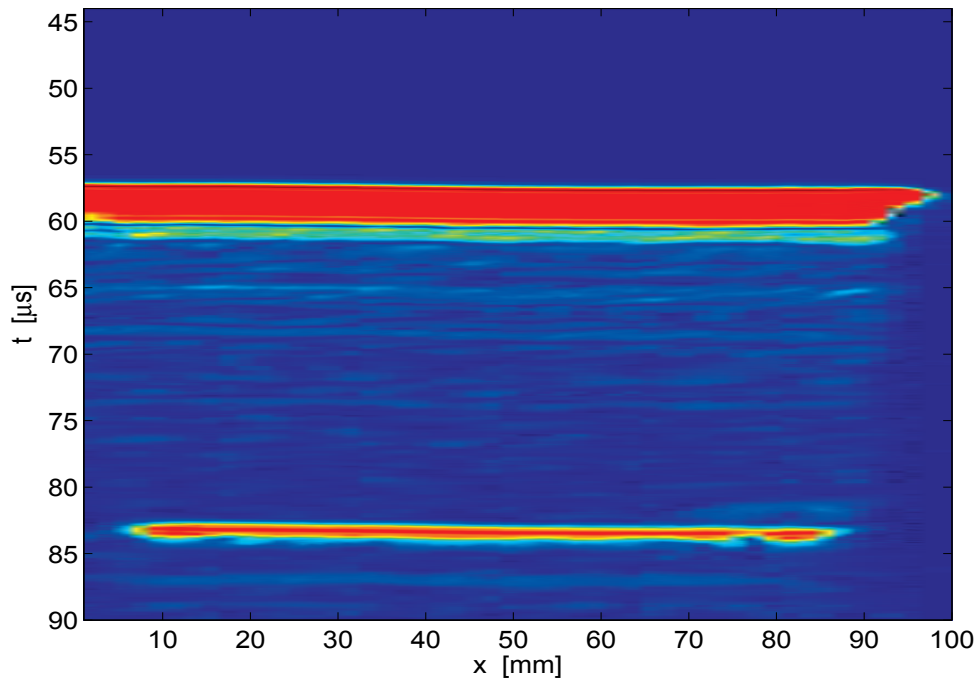


Figure 4.7: Original B-scan acquired at $y = 18$ mm passing over the 1 mm and 4 mm FBHs.

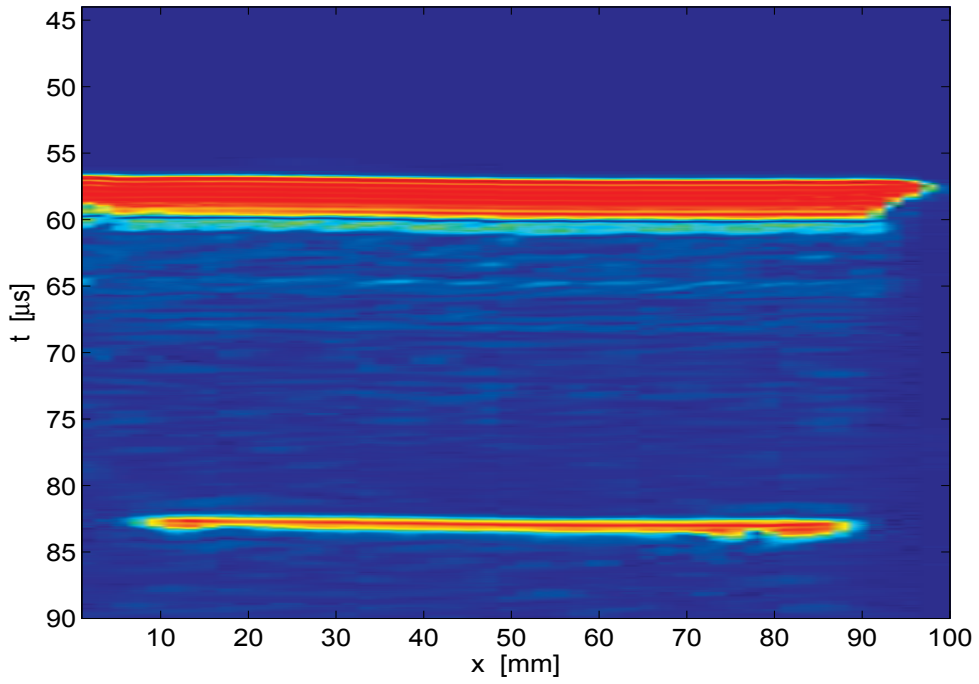


Figure 4.8: Original B-scan acquired at $y = 63$ mm passing over the 3 mm and 2 mm FBHs.

In Figure 4.9, the migrated image corresponding to the B-scan in 4.7 is presented. The 4 mm FBH at $z \approx 97$ mm is here reduced to approximately 5 mm.

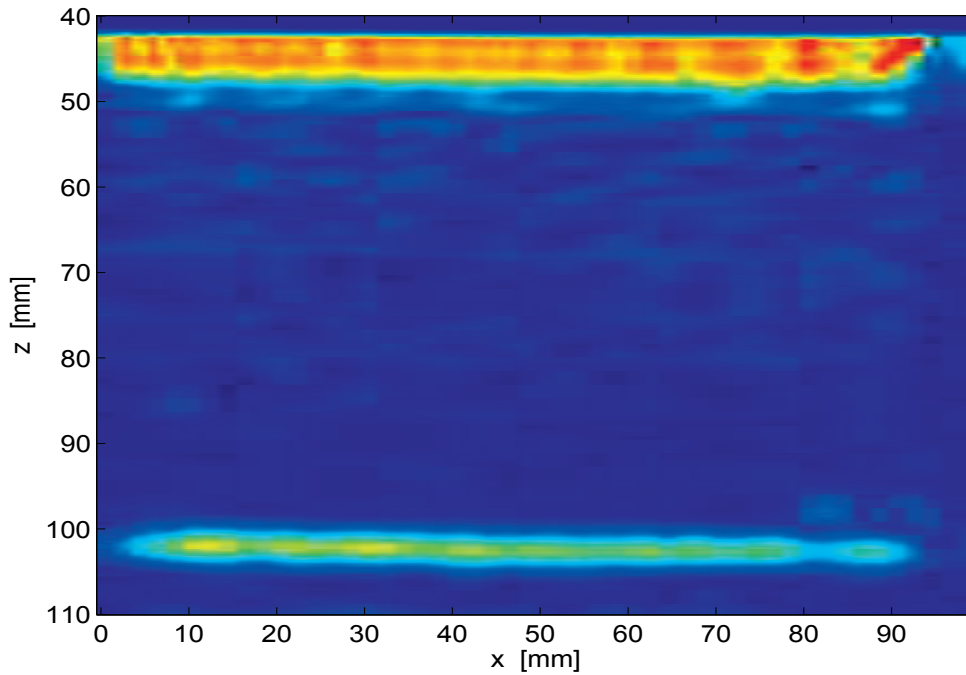


Figure 4.9: Image obtained by migration of the B-scan in Figure 4.7.

In a similar way, the migrated image corresponding to the B-scan in 4.8 is presented in Figure 4.10. The 3 mm and 2 mm FBHs FBH at $z \approx 97$ mm are better localized in the x -direction

thus providing better conditions for extracting a C-scan.

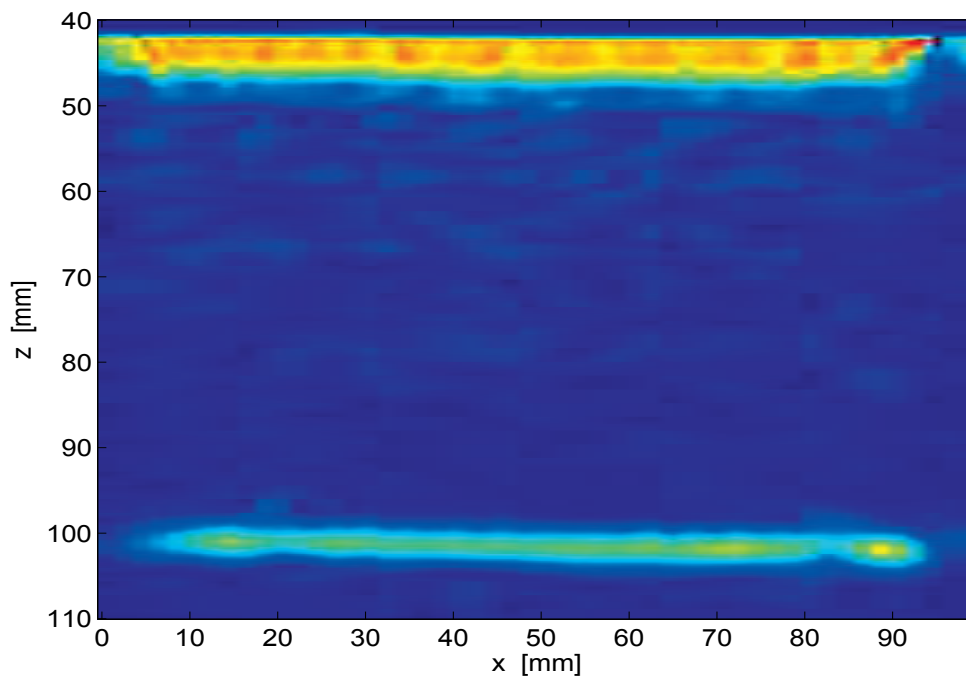


Figure 4.10: Image obtained by migration of the B-scan in Figure 4.8.

A C-scan image showing a cross section of the block at a z interval $[95, 99]$ mm, corresponding to $53 - 57$ mm in the Cu-block, is presented in Figure 4.11. The C-scan was obtained by projecting the maximum amplitude value within the given interval onto the $x - y$ plane. This C-scan should be compared to the C-scan shown in Figure 4.12, which was created using images that were migrated in the x -direction. The FBHs of diameters 2, 3, and 4 mm are visible in both images but the resolution is much improved in the migrated C-scan. Note that the improvement in resolution only concerns the direction of migration; the resolution in the y -direction is approximately the same in both images.

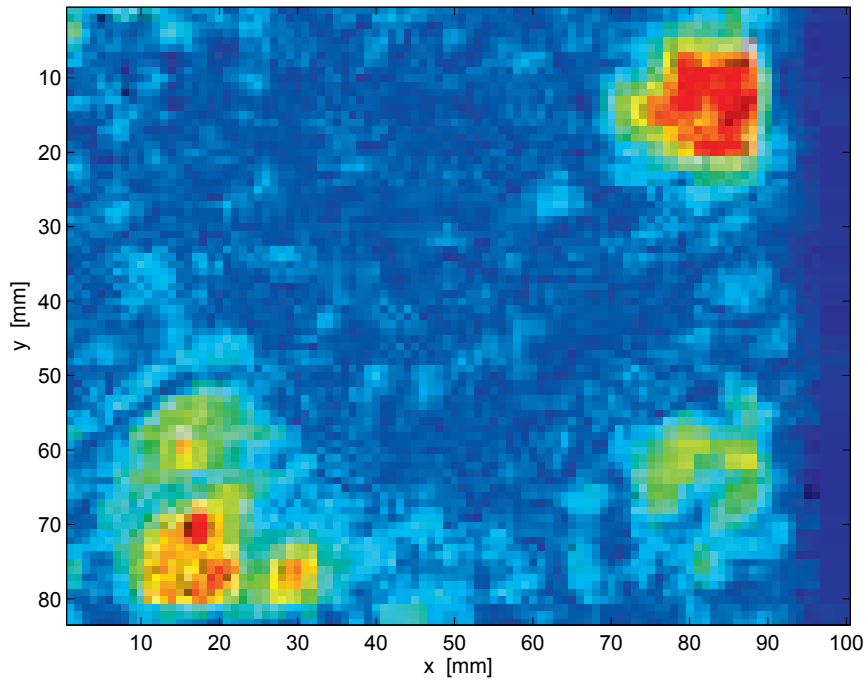


Figure 4.11: C-scan based on raw data.

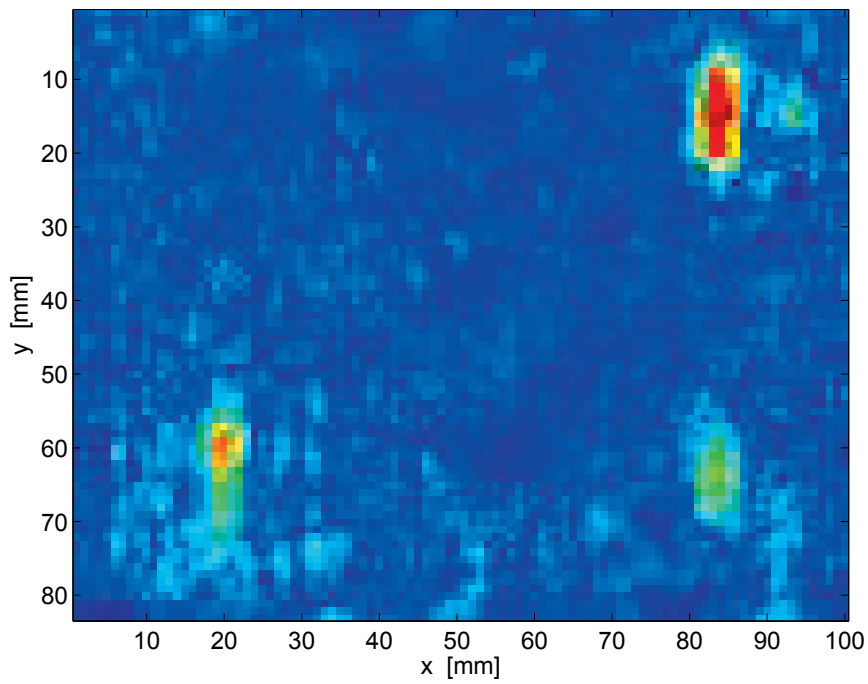


Figure 4.12: C-scan based on migrated data.

A number of profile plots covering cross-sections over the FBHs are shown in Figure 4.13.

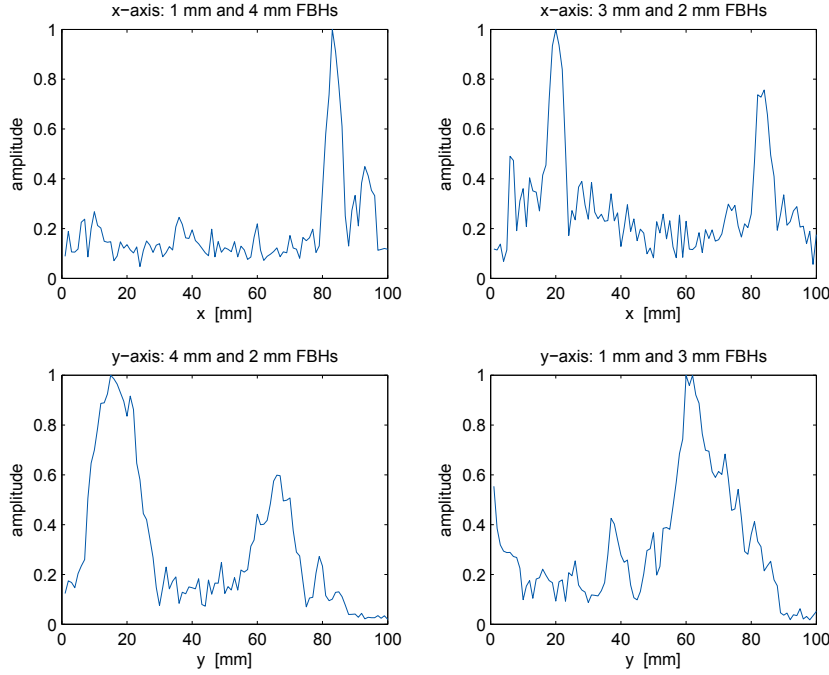


Figure 4.13: Profile plots based on migrated data. Each profile has been normalized to have unit maximum amplitude. The two upper plots show profiles taken along the x -axis, in which migration was performed, and the lower show profiles in the y -direction.

4.4 Conclusions and discussion

Phase shift migration algorithm has been proposed for ultrasonic imaging of solids immersed in water. The proposed algorithm has been demonstrated to correctly treat ultrasonic waves propagating through layered media with different velocities and to yield images with a high lateral resolution under such conditions.

The experiment with the copper block with SDHs, showed that the lateral resolution in the reconstructed image is independent of depth to a good approximation. It was also demonstrated using data from a block with FBHs that the phase shift migration along with the resolution improvement helps in suppressing grain noise and thus is a useful tool for the detection of defects that are buried deep in grainy materials.

The algorithm is implemented using FFT routines and the current implementation allows processing of the B-scans that takes less time than the data acquisition. We should note here that little effort has been made to optimize the efficiency of the code and that the algorithm can be speeded up significantly in at least one way. The current implementation does not take into account that the acquired signals are relatively narrow-band which means that a large number of Fourier coefficients can be neglected in the calculations. By doing this and investigating other ways to improve the code, we will open up for the possibility to perform also 3D migration, something that which will be a topic for future work.

The phase migration technique requires the knowledge of the sound velocities in the different media involved in the test. We have here considered only the two media, water and copper but there are no principal restrictions on how many layers we can treat using the method as long as they are all horizontal. It is of course important to supply the algorithm with the correct velocity values since incorrect values will lead to both poor resolution and poor geometrical correction

of the images. Fortunately, there are fairly simple means to verify that the velocity values are correct. We can easily label each image line with the velocity used for the reconstruction of the particular line and this label can be compared with the overall structure of the image such as the location of front surface and back surface echoes. This requires precise information on the initial delay of the acquired signals but such information is supported as a standard in modern ultrasonic systems.

Bibliography

- [1] M. Soumekh. *Synthetic Aperture Radar Signal Processing with Matlab Algorithms*. John Wiley & Sons, 1999.
- [2] K.J. Langenberg, M. Berger, T. Kreutter, and K. Mayer. Synthetic aperture focusing technique signal processing. *NDT International*, 19(3):177–189, June 1986.
- [3] K. Mayer, R. Marklein, K. Langenberg, and Th. Kreutter. Three-dimensional imaging system based on Fourier transform synthetic aperture focusing technique. *Ultrasonics*, 24(4):241–255, July 1990.
- [4] T. Stepinski. An implementation of synthetic aperture focusing techniques in frequency domain. *IEEE Trans. on Ultrasonics, Ferroelectronics and Frequency Control*, 54(7):1399–1408, July 2007.
- [5] T. Stepinski (editor), T. Olofsson, and Erik Wennerström. Inspection of copper canisters for spent nuclear fuel by means of ultrasound. Technical report, 06-47. Department of Engineering Sciences, Uppsala University, 2006.
- [6] J. Claerbout. Basic earth imaging. URL: <http://sepwww.stanford.edu/sep/prof>, 2005.
- [7] J.F. Claerbout. Coarse grid calculations of waves in inhomogeneous media with application to delineation of complicated seismic structure. *Geophysics*, 35(3), June 1970.
- [8] R. Stolt. Migration by fourier transform. *Geophysics*, 43(1):23–48, 1978.
- [9] J. Gazdag. Wave equation migration with the phase-shift method. *Geophysics*, 43(7):1342–1351, December 1978.
- [10] K. Gu, G. Wang, and J. Li. Migration based SAR imaging for ground penetrating radar systems. *IEE Proceedings: Radar, Sonar and Navigation*, 151(5):317–325, October 2004.

4.A Appendix

Comments on the use of the discrete Fourier transform and aliasing

All Fourier transforms involved in the algorithm are performed using discrete data and the fast Fourier transform (FFT) has been used for all calculations. The problem of aliasing may then appear both spatially and temporally. The temporal sampling must fulfil the Nyquist criterion, stating that the sampling frequency must at least be twice that of the highest frequency appearing in the signals. This requirement is fulfilled with a large margin in the experiments presented in Section 4.3; the sampling frequency was 100 MHz whereas the center frequency of the transducer was 2.25 MHz and its bandwidth was approx. 1.5 MHz.

The spatial sampling of the x -axis is more critical. In its conventional form, in which a scenario with constant velocity is considered, the spatial sampling theorem states that two sampling points on the x -axis, Δx , should be separated by no more than $\lambda_{min}/4$ for pulse-echo measurements where λ_{min} is the minimum wave length appearing in the measurements.

An example: If we use a transducer with an upper frequency of 3 MHz for the measurements in water, having a velocity of 1500 m/s, we have that $\lambda_{min} = 0.5$ mm and $\Delta x < 0.125$ mm which is a quite small separation that will lead to impractical data acquisition times if large areas are to be scanned.

The requirement $\Delta x < \lambda_{min}/4$ is however quite overpessimistic and does not take into account the transducer's beampattern. If this is done, we arrive at the much less restrictive result stating that when a circular transducer of diameter D is used, the spatial sampling should be performed at steps no longer than $\Delta x < D/4$ [1]. For a transducer of 10 mm we thus have that $\Delta x < 2.5$ mm which is fulfilled in our measurements.

We note that Δx is independent of frequency and this is related to the fact that the diffraction angle becomes smaller as the frequency increases. The spatial aliasing is connected to the change in time delay between a scatterer at two consecutive measurements, or in other words, the slope of the hyperbolic response from a scatterer. This slope increases as the distance between scatterer and transducer in the x -direction increases but since smaller sections of these hyperbolas are "seen" by the transducer at higher frequencies, the time delay that effectively determines the spatial sampling becomes smaller as the frequency increases. This decrease turns out to exactly compensate the increased anti-aliasing demands with increasing frequency (the λ -dependence).

Finally, aliasing can occur also when performing the inverse transform back to spatial coordinates. The Fourier coefficients are essentially connected to a function that is periodic both in t and x and especially the periodicity in x may cause problems in the reconstruction. The problem can be avoided by using zero-padding of the measured data in the x -direction and to find how much zero padding should be used, we here take a practical standpoint, suggested in [10], in which we increase the number of padded zeros, N_x , to a point where we no longer see a difference between the images reconstructed using different N_x .

